*ob*ABPP-HT*: A Precision-Engineered Activity Proteomics Pipeline for the Streamlined Discovery of Deubiquitinase Inhibitors

Hannah B. L. Jones[1*Δ], Simeon D. Draganov[1,2Δ], Sofia Schönbauer Huamán[3], Peter A. C. Wing[2], Chuong Nguyen[4], Zhu Liang[1,2,9], Julia Dörner[3], Jasper Lithgow[3], Emma Murphy[1], Alice Beard[1,2], Andrea Pierangelini[1], Jack W. Houghton[5], Mackenzie E. Robert[6], Sarah Flannery[1], Anthony Tumber[3], Iolanda Vendrell[1], Edward W. Tate[5], Paul R. Elliot[7], Graham M. West[4], Darragh P. O'Brien[1], Eidarus Salah[3], Andrew P. Turnbull[8], Christopher J. Schofield[3], Benedikt M. Kessler[1,2], Lennart Brewitz[3*], and Adán Pinto-Fernández[1,2*]

Affiliations:

[1]Target Discovery Institute, Centre for Medicines Discovery, Nuffield Department of Medicine, University of Oxford, Oxford, United Kingdom.

[2]CAMS Oxford Institute and Centre for Medicines Discovery, Nuffield Department of Medicine, University of Oxford, Oxford, United Kingdom.

[3]Chemistry Research Laboratory, Department of Chemistry and the Ineos Oxford Institute for Antimicrobial Research, University of Oxford, Oxford, United Kingdom.

[4]Hit Discovery and Optimization (HDO) Pfizer Inc. Groton, Connecticut, United States of America.

[5]Department of Chemistry, Molecular Sciences Research Hub, Imperial College London, London, United Kingdom.

[6]Discovery Biology and Pharmacology, Pfizer Inc. Groton, Connecticut, United States of America.

[7]Department of Biochemistry, University of Oxford, Oxford, United Kingdom.

[8]Cancer Research Horizons, Francis Crick Institute, London, United Kingdom

[9]Present address: Department of Microbiology, Harvard Medical School, Boston, Massachusetts, United States of America.

Equal contributions: Δ

*Correspondence: Hannah B.L. Jones, Lennart Brewitz, and Adán Pinto-Fernández

Abstract (140 / 150 words)

Deubiquitinases (DUBs), and the dysregulation thereof, are implicated in human disease. The recent inclusion of selective DUB inhibitors in clinical trials has heightened interest in DUB-focused drug discovery. Current DUB screening methods remain constrained, however, as they often rely on recombinant proteins that are truncated or derived from non-human sources, typically necessitating extensive optimisation of initial hits. We introduce a high-throughput, endogenous human DUB-focused activity proteomics workflow designed for the simultaneous screening and profiling of small, targeted libraries of catalytic group-reactive compounds. In a proof-of-concept screen, this innovative platform expanded the repertoire of electrophilic groups targeting DUBs, leading to the discovery of potent and selective inhibitors for USP47, OTUD7B, and USP5. Remarkably, these inhibitors required minimal or no optimisation to confirm the previously reported biological roles of the three DUBs, underscoring the advantages of this methodology for drug discovery applications.

42 ## Main

43 Post-translational ubiquitylation regulates key cellular processes, including protein and
44 organelle homeostasis, through the interplay of ubiquitinating and deubiquitinating
45 machineries[1–4]. Deubiquitinases (DUBs), primarily nucleophilic cysteine enzymes, cleave Ub
46 from biomolecules, mainly proteins, modulating their fate[5,6]. Dysregulated DUB functions are
47 linked to diseases and are tractable therapeutic targets[1]. Small-molecule USP1 and USP30
48 inhibitors are in clinical trials for cancer[7,8], chronic kidney disease[9], and Parkinson's disease,
49 for example[3,10].

50 Activity-based probes (ABPs) targeting nucleophilic cysteine DUBs have been developed[11–14].
51 We and others have designed assays using a haemagglutinin (HA)-tagged, ubiquitin-based
52 DUB ABP with a propargylamine (PA) warhead (HA-Ub-PA) to assess inhibitor potency and
53 selectivity across endogenous DUBs, whilst also providing information on cellular
54 permeability, and stability[15–17]. DUB activity proteomics, or activity-based protein profiling
55 (ABPP), uses affinity purification in combination with liquid chromatography-tandem mass
56 spectrometry (LC-MS/MS) to analyse DUB–ABP complexes. Unlike recombinant enzyme
57 assays, ABPP evaluates ligand binding to endogenous, unmodified proteins in a cellular
58 environment, supporting the discovery of selective inhibitors, including those for challenging
59 targets[18,19].

60 ABPP's broader applicability was historically limited by low sensitivity and throughput, due to
61 labour-intensive workflows encompassing ABP labelling, purification, sample preparation, MS
62 analysis, and data processing. To enhance its utility for DUB inhibitor discovery, we previously
63 increased throughput by adapting the probe purification step to a 96-well plate format,
64 integrating an automated liquid handling system (Agilent Bravo) with ultra-fast, sensitive LC–
65 MS/MS instrumentation (Evosep-timsTOF). This method (ABPP-HT) facilitated analysis of
66 ~100 samples daily[20]. We subsequently enhanced the sensitivity of ABPP-HT by incorporating
67 data-independent acquisition LC-MS/MS (DIA), enabling deeper and more comprehensive
68 DUBome profiling (ABPP-HT*)[21]. Further improvements aimed at enhancing sensitivity
69 included using diverse Ub probe approaches, high-pH pre-fractionation[22], and isobaric
70 labelling (Extended Data Fig. 1 a–e).

71 Here, we present an on-bench version of the ABPP-HT* workflow, named "*ob*ABPP-HT*",
72 which maintains the throughput and sensitivity of ABPP-HT* without requiring automated
73 platforms for ABP immunoprecipitation. We used *ob*ABPP-HT* to screen a curated small-
74 molecule library enriched in cysteine-reactive scaffolds and substrate mimetics. This resulted
75 in the discovery of selective inhibitors for USP47, OTUD7B, and USP5, which were
76 subsequently validated in biochemical and cellular assays. Our findings showcase *ob*ABPP-
77 HT* as a widely accessible platform and the utility of using advanced activity proteomics to
78 accelerate DUB inhibitor discovery and development.

79 ## Results

80 **Development of a Flexible ABPP-HT Methodology for Broad Applicability**

81 To enhance accessibility, the *ob*ABPP-HT* workflow incorporates magnetic beads and a multi-
82 well magnetic rack, circumventing the need for highly specialised equipment (Fig. 1a).
83 Compared to our Bravo robot protocol, *ob*ABPP-HT* enables greater DUBome depth (Fig. 1b),
84 enriching in excess of 40 DUBs in the same MCF-7 cell line (Fig. 1c-e). This may be a result of
85 extended binding times during affinity purification. The high-throughput approach uses a
86 single-shot DIA method with 11 min gradients on an Evosep-timsTOF LC-MS/MS, enabling
87 analysis of approximately 100 samples per day. For laboratories lacking elements of this
88 setup, increased throughput can also be achieved through TMT-based multiplexing, which has
89 been previously incorporated into DUB ABPP[18] (Extended Data Fig. a-c).

90 We further validated the versatility of *ob*ABPP-HT* by translating it onto a Thermo KingFisher
91 Apex purification system (Fig. 1a), using two different ABPs (HA-Ub-PA and bio-ISG15-PA), in
92 a second cell line (HAP1)[20,23,24]. In this configuration, the Ub probe captured DUB profiles
93 (Extended Data Fig. 1f, 1g) comparable to the on-bench method, while the ISG15 probe
94 selectively reacted with known deISGylases, including USP5, USP14, USP16, USP18 and
95 USP36[23,25] (Extended Data Fig. 1h).

96 ***ob*ABPP-HT* for DUB Inhibitor Identification**

97 We demonstrated the utility of the *ob*ABPP-HT* workflow for the discovery of DUB inhibitors
98 by investigating a curated library of small-molecules capable of reacting with nucleophilic
99 cysteine enzymes (Fig. 1f). These included αβ,α'β'-diepoxyketones (DEKs), some known to

100 covalently react with nucleophilic cysteine enzymes[26], γ-lactams, with examples reported to
101 covalently react with the SARS-CoV-2 main protease[27], and Ub-derived oligopeptides
102 specifically designed for this study, bearing either a C-terminal nitrile or alkyne group (Table
103 S1-3).

104 Small-molecules (25 µM) were incubated with MCF-7 breast cancer cell lysates in a 96 well
105 plate, enabling the profiling of 41 compounds and FT827, a well-characterised DUB inhibitor[28],
106 in technical duplicates. The plate also included negative/positive controls (−/+ HA-Ub-PA).
107 Across replicates, 38 DUBs were consistently enriched >5-fold, with an average coefficient of
108 variation (CV) of 16%, confirming robustness (Extended Data Fig. 2a). Reassuringly, *ob*ABPP-
109 HT* replicated the known potent and selective USP7 inhibition by FT827[28]. Eight compounds
110 significantly inhibited at least one DUB (>20% intensity loss, $p < 0.05$; Fig. 2a). Of these,
111 **Compounds 4** and **27** were excluded due to a lack of selectivity. Selective hits included:
112 **Compound 3** (USP47 > USP7), **Compound 6** (OTUD7B), **Compound 7** (USP30/USP47/VCPIP1),
113 **Compound 25** (USP5), and **Compounds 26** and **32** (USP33) (Fig. 2b, 2c). Notably, USP5-
114 selective alkyne 25 is a diastereomer of cross-reactive alkyne 27, highlighting the workflow's
115 ability to resolve isomer-specific effects. (Extended Data Fig. 2b, 2c).

116 **Hit Validation and Dose-Response Analysis**

117 Western blots confirmed inhibition of USP47/USP7 by **Compound 3**, OTUD7B by **Compound**
118 **6**, and USP5 by **Compound 25** (Fig. 2d). DUB inhibition was concentration-dependent (Fig. 2e)
119 and IC_{50} values revealed the preference of **Compound 3** for USP47 (8.8 µM) over USP7 (36
120 µM) (Fig. 2f), which was consistent with screening data. **Compounds 26** and **32** were deemed
121 false positives (Extended Data Fig. 2d), while **Compound 7** induced protein crosslinking and/or
122 aggregation, likely due to its bifunctional epoxide structure (Extended Data Fig. 2e)[26]. To
123 assess the stability of binding, **Compounds 3**, **6**, and **25** were pre-incubated with MCF-7
124 lysates before probe addition and incubated for 5, 15, or 45 min. Minimal inhibitor
125 displacement by HA-Ub-PA was observed (Extended Data Fig. 2f–i), suggesting irreversible
126 binding at DUB active sites.

127 **DUB Inhibitor Selectivity Assessment by *ob*ABPP-HT***

128 Due to its increased throughput capabilities, the *ob*ABPP-HT* workflow was also used to
129 assess the selectivity of inhibitors **3**, **6**, and **25** across several concentrations (Fig. 3a-f). The

130 dose-dependent inhibition curves and IC_{50} values for the three compounds were comparable
131 to those generated by immunoblotting (Extended Data Fig. 3 a-d)[20]. **Compound 3** exclusively
132 inhibited USP47 and USP7 up to 50 µM, with weak USP40 inhibition being observed at higher
133 doses (Fig. 3a, 3d). The inhibition profile of **Compound 3** was consistent when tested in HAP1
134 cells using the KingFisher purification system (Extended Data Fig. 3e). **Compound 6** was
135 selective for OTUD7B up to 100 µM but also affected USP16 and USP28 at 250 µM (Fig. 3b,
136 3e). Notably, **Compound 25** was highly selective, only inhibiting USP5 across the tested
137 concentration range (Fig. 3c, 3f).

138 The active sites of DUBs and deISGylases are structurally similar and most deISGylating
139 enzymes are cross-reactive DUBs, cleaving both Ub and ISG15, with the notable exception of
140 USP18[23–25,29]. Given USP5's dual Ub/ISG15 specificity, we evaluated the effect of **Compound**
141 **25** on deISGylases by immunoblotting, using the bio-ISG15-PA ABP. Remarkably, **Compound**
142 **25** inhibited USP5 to a similar extent as with the Ub ABP, and did not cross-react with USP18
143 or any of the other detected deISGylases in the tested concentration range (up to 125 µM),
144 further demonstrating its high selectivity (Extended Data Fig. 3f). It is important to note that
145 both **Compounds 3** and **6** are also reported to weakly inhibit the mycobacterial L,D-
146 transpeptidase Ldt_{Mt2} and the SARS-CoV-2 main protease[26], implying that they may also react
147 with additional human nucleophilic cysteine enzymes other than DUBs.

148 **Cell Permeability and Inhibitor Optimisation**

149 We assessed cell permeability of the identified DUB inhibitors by treating intact MCF-7 cells
150 prior to probe labelling. **Compounds 3** and **6** were cell-permeable and inhibited USP47/USP7
151 and OTUD7B, respectively, in a concentration-dependent manner (Fig. 3g, 3h). **Compound 3**
152 induced toxicity at the highest concentration (250 µM), suggesting off-target effects.
153 **Compound 25**, however, was inactive in intact cells (Fig. 3i, 3j). To optimise **Compound 25** for
154 cellular activity, we modified the alkyne and amine protecting groups. Substituting the
155 terminal alkyne reduced potency (Fig. 3k; Extended Data Table 1; synthesis detailed in SI),
156 supporting that **Compound 25** covalently reacts with the USP5 nucleophilic cysteine via its
157 alkyne group. By contrast, altering amine-protecting groups at the N-terminus (R_1) and/or at
158 the N^{ϵ}-lysine amino group (R_2), led to two active derivatives, **25a** and **25b**, with
159 trifluoromethyl groups at R1 and trifluoroacetyl (**25a**) or *tert*-butyloxycarbonyl (Boc; **25b**) at
160 R2 (Fig. 3l). Both derivatives retained the potency and selectivity observed in lysates

161 (Extended Data Fig. 4a), offering promising leads for functional studies or therapeutic
162 development.

163 **Molecular Basis of Compound 3 Preference for USP47**

164 Reported USP47 inhibitors inhibit USP7 with comparable potency[30,31], likely reflecting their
165 highly related phylogeny and homology[29,32]. Given the preference of **Compound 3** for USP47
166 over USP7, we decided to use it as a tool to further investigate its mode of action and
167 elucidate molecular differences between the two DUBs. In fluorogenic ubiquitin-rhodamine
168 (Ub-Rho) biochemical assays, **Compound 3** showed ~10-fold more activity for recombinant
169 USP47 over recombinant USP7 after 30 min preincubation (IC_{50}: 0.48 vs. 4.3 µM; Fig. 4a,
170 Extended Data Fig. 5a–d). Time-dependency experiments indicated covalent or slow tight-
171 binding inhibition for USP47 (Fig. 4c), while USP7 inhibition was weaker and time-
172 independent (Fig. 4b). For both enzymes, progress curves in the presence of **Compound 3**
173 were non-linear indicating slow initial binding (Extended Data Fig. 5e, 5f).

174 Human USP47 shares 43% sequence identity to human USP7 within the catalytic domain. In
175 the absence of a human USP47 Protein Data Bank (PDB) structure, the structure of human
176 USP7 in complex with the covalent inhibitor, FT827 (PDB: 5NGF), was used as the template to
177 generate a homology model of human USP47 with an appropriate conformational state for
178 covalent inhibitor docking studies. **Compound 3** most likely forms a covalent adduct with the
179 catalytic cysteine of human USP47 (C197) via 1,2-carbonyl attack and retro-aldol
180 fragmentation based on previously reported work (Extended Data Fig. 5g)[26].

181 Docking studies suggest that **Compound 3** binds in the thumb-palm cleft (Extended Data Fig.
182 5h) and sterically blocks Ub binding (Extended Data Fig. 5i), analogous to the covalent USP7
183 inhibitor, FT827 (PDB: 5NGF; Extended Data Fig. 5j). The binding site is flanked by 14 residues
184 including R402, which is predicted to form a key hydrogen bonding interaction with the
185 epoxide moiety of **Compound 3** (Fig. 4d). In human USP7, the substitution of R402 with an
186 asparagine residue (N418), which has a shorter side chain and cannot interact with the
187 compound, may explain the higher potency of **Compound 3** for USP47 (Fig. 4e).

188 USP47 apoform (PDB: 8ITN) and Ub-bound (PDB: 8ITP) structures exist for the closely related
189 catalytic domain of *C. elegans* USP47 (44% sequence identity). A comparison of the human
190 USP47-**Compound 3** model with apoform *C.elegans* USP47 suggests that **Compound 3** binding

191 disrupts hydrogen bonding between R402 and H271, which is involved in stabilising the
192 switching loop "in", catalytically incompetent conformation, thereby promoting an active,
193 switching loop "out" conformation compatible with activation peptide binding as observed in
194 USP7's regulatory mechanism (Extended Data Fig. 5o, 5p)[33,34].

195 Hydrogen-deuterium exchange mass spectrometry (HDX-MS) analysis confirmed differential
196 binding modes (Fig. 4f, 4g, and Extended Data Fig. 5k, 5l), revealing conformational shifts
197 indicative of a switching loop rearrangement in USP47 (Extended Data Fig. 5m) and potential
198 engagement of the activation peptide (Fig. 4h)[34]. Notably, HDX-MS for USP7 showed no such
199 distal conformational changes, indicating that **Compound 3** does not promote equivalent
200 switching loop reorganisation or activation peptide binding in USP7 (Fig. 4i and Extended Data
201 Fig. 5n). These differences likely underpin **Compound 3**'s selectivity for USP47.

202 **Compound 3 Inhibits the NLRP3 Inflammasome**

203 Both USP7 and USP47 are reported to regulate the NLRP3 inflammasome[32]. When inducing
204 inflammasome activation with lipopolysaccharide (LPS) and nigericin in human monocyte cells
205 (THP-1), treatment with **Compound 3** at low concentrations increased viability and reduced
206 inflammasome-mediated pyroptosis (Extended Data Fig. 6a, 6b), suggesting inflammasome
207 suppression. In contrast, high concentrations and prolonged nigericin exposure induced
208 toxicity, consistent with additional targets beyond DUBs[26]. Importantly, at shorter nigericin
209 incubation times, **Compound 3** inhibited inflammasome activation, as evidenced by reduced
210 Caspase-1 activity (Fig. 5a, Extended Data Fig. 6 c-e), blocked oligomerisation of apoptosis-
211 associated speck-like protein containing a CARD (ASC), and prevented cleavage of Caspase-1,
212 IL-1β, and gasdermin D (GSDMD) (Fig. 5a, 5b). Intriguingly, while we observed a decrease in
213 NLRP3 levels, the treatment of cells with **Compound 3** triggered the appearance of a high
214 molecular weight NLRP3 smear, consistent with ubiquitylation (Fig. 5b).

215 **Compound 6 Induces HIF-1α Degradation via OTUD7B Inhibition**

216 OTUD7B has been shown to regulate Hypoxia-Inducible Factor 1 (HIF-1α) protein homeostasis
217 in hypoxia in a von Hippel-Lindau disease tumour suppressor (VHL)- and proteasome-
218 dependent manner[35]. In hypoxic Calu-3 cells, **Compound 6** reduced HIF-1α in a dose-
219 dependent manner (Fig. 5c). In renal carcinoma cells lacking active VHL (RCC4-VA)[36], we
220 observed that treatment with **Compound 6** had no impact on HIF-1α expression. When wild-

221 type VHL (RCC4-VHL) expression was restored, however, a dose-dependent reduction in
222 hypoxic HIF-1α expression was observed (Fig. 5d). In HAP1 WT cells, treatment with
223 **Compound 6** also resulted in a dose-dependent reduction in HIF-1α expression. Importantly,
224 HIF-1α levels were markedly reduced in OTUD7B KO cells compared to WT, consistent with
225 published findings[35]. Treatment of KO cells with **Compound 6** did not further reduce HIF-1α,
226 supporting an on-target mechanism (Fig. 5e). In line with reported work[37], we demonstrated
227 that incubation of infected Calu-3 cells in hypoxia restricted replication of SARS-CoV-2, yet
228 treatment with **Compound 6** limited the antiviral impact of hypoxia (Fig. 5f), consistent with
229 limited HIF-1α expression through inhibition of OTUD7B.

230 **Compound 25b is a Potent Anti-Viral Against SARS-CoV-2**

231 The functions of USP5 in viral replication have been linked to type I interferon (IFN-I)
232 production by regulating the ubiquitylation of different innate immune factors such as RIG-I
233 and IRF3[38,39]. In agreement with these observations, treatment of cells with the synthetic RNA
234 Poly I:C induced IFN-I production, which was significantly amplified by co-treatment with
235 **Compound 25b** (Fig. 5g)[39,40]. **Compound 25b** exhibited a dose-dependent reduction in viral
236 replication against SARS-CoV-2 in infected Calu-3 cells. In comparison to remdesivir, a
237 guanosine nucleoside analogue which targets the viral replicase complex and is in clinical use
238 as a broad-spectrum antiviral medication, **Compound 25b** showed a ~10-fold increase in
239 potency (Fig. 5h). Interestingly, **Compound 25b** did not show any significant toxicity at
240 concentrations as high as 200 µM (Extended Data Fig. 7a).

241 ## Discussion

242 As interest in DUBs as drug targets grows[6,40,41], so does the need for better methodologies to
243 identify DUB inhibitors. High-throughput screening (HTS) has been instrumental in DUB drug
244 discovery by enabling the rapid evaluation of extensive compound libraries[28,42]. However, HTS
245 is typically limited by high costs, low hit rates, reliance on less disease-relevant recombinant
246 proteins, and *in vitro* assays that may not reflect physiological conditions. It also typically
247 requires extensive compound optimisation and follow-up validation due to identification of
248 false and/or not selective hits.

249 To address these challenges, artificial intelligence (AI) and activity-based proteomics have
250 emerged as promising alternatives. AI-enabled virtual screening approaches, exemplified by

251 AtomNet, streamline early-stage discovery by computationally assessing compound-target
252 interactions prior to synthesis, even in the absence of prior ligand data[43]. Similarly, using
253 dedicated activity proteomics strategies for the unbiased identification and mapping of
254 reactive cysteine residues in the human proteome has allowed directed, more efficient drug
255 design for cysteine-containing proteins, including DUBs[44–47]. Importantly, recent progress in
256 DUB ABPP has produced high-throughput-ready platforms, unlocking new opportunities for
257 small-molecule screening[18,20,48].

258 Here, we describe the *ob*ABPP-HT* activity proteomics workflow. *ob*ABPP-HT* is cost-
259 effective, requiring no specialised equipment, however, it can seamlessly integrate with
260 automation systems like the Thermo KingFisher Apex and Agilent Bravo, and is compatible
261 with different probe types, enabling profiling of enzyme classes other than DUBs. This high-
262 throughput and highly sensitive method enables the analysis of ~100 samples per day using
263 EvoSep timsTOF LC-MS/MS.

264 As a proof-of-concept, we screened for mechanistically novel DUB inhibitors by combining
265 *ob*ABPP-HT* with a curated small-molecule library composed of molecules that bear
266 electrophilic warheads for potential covalent reaction with cysteine residues, including
267 αβ,α′β′-diepoxyketones (DEKs), γ-lactams, and ubiquitin-derived peptide inhibitors
268 specifically designed for this study. This screen showed a hit rate ~10-times higher than
269 traditional DUB HTS and, after hit validation, identified new inhibitors against USP47,
270 OTUD7B, and USP5. The potential of these DUBs as drug targets has not yet been fully
271 explored; therefore, the potency, cellular permeability, selectivity, and functional effects of
272 the identified DUB antagonists was further characterised.

273 USP47 is an attractive therapeutic target[49–51]. However, reported USP47 inhibitors also inhibit
274 USP7 with comparable potency[30,31], attributable to their high homology[29,32]. We identified
275 **Compound 3**, a first-in-class USP47 inhibitor with preference for USP47 over USP7, an
276 observation which was confirmed using orthogonal kinetic studies, and characterised through
277 HDX-MS-based mapping and molecular docking studies, revealing the molecular basis for
278 selective USP47 inhibition. Importantly, USP47/7 inhibition and knockdown has previously
279 been demonstrated to prevent inflammasome activation[32], a finding that is recapitulated by
280 **Compound 3** treatment.

281 Although roles of OTUD7B in disease remain to be comprehensively investigated[52], evidence
282 suggests that OTUD7B is a potential therapeutic target[35,53–55]. This interest is highlighted by
283 recent reports detailing the development of OTUD7B inhibitors[48,56]. We identified **Compound**
284 **6**, a potent, permeable, stable and selective OTUD7B inhibitor which was able to reduce HIF-
285 1α levels under hypoxic conditions[37], phenocopying OTUB7B knockdown studies[35]. Recently,
286 hypoxia has been described to impact the ability of SARS-CoV-2 to infect cells in a HIF-1α-
287 dependent manner[37,57]. In line with its effects on HIF-1α stability, **Compound 6** rescued SARS-
288 CoV-2 infectivity in hypoxia[57].

289 USP5 catalyses hydrolysis of free poly-ubiquitin chains, with its zinc finger ubiquitin binding
290 domain (ZnF UBP) containing a pocket to bind the C-terminal di-glycine motif on ubiquitin[58].
291 Although USP5 is a potential target for treatment of cancer, pain, and inflammation[59], only
292 limited structure-activity relationship studies on USP5 inhibitors have been reported (Fig. S1)
293 and lack characterisation in a cellular context[60]. Existing USP5 inhibitors were designed based
294 on the Ub C-terminus and thus contain a carboxylate group to mediate binding to the USP5
295 ZnF[60,61]. By contrast, we achieved selective USP5 inhibition using Ub-derived inhibitors in
296 which the C-terminal glycine is substituted for a propargyl group, based on the observation
297 that Ub-PA can covalently react with nucleophilic DUB cysteine thiols[54]. The identified
298 **Compound 25** exhibits high levels of selectivity for USP5 inhibition over related DUBs USP16
299 and USP22[62]. That relatively simple substrate-derived molecules like **Compound 25** exhibit
300 high selectivity for individual DUBs is remarkable, highlighting subtle but critical differences
301 in active site architecture. **Compound 25** likely covalently modifies the nucleophilic cysteine
302 of USP5 via its alkyne warhead, as supported by reported crystal structure of USP5 in complex
303 with a Ub-derived probe (PDB: 3IHP[63]), the structures of related USPs with Ub-PA, and the
304 observed reduced inhibition upon steric hindrance by introducing sterically bulky substituents
305 near the alkyne. The selectivity of **Compound 25** for USP5 may arise from USP5's unique
306 domain architecture. A disulphide bridge between C793 (BL2) and C195 (cUBP) in the USP5-
307 Ub complex may limit BL2 flexibility, positioning cUBP near the binding site and enabling
308 additional compound interactions. C195 may also affect dimerization, further shaping
309 compound engagement. The use of a latent electrophile for covalent reaction with the active
310 site cysteine may also result in improved USP5 selectivity, potentially due to the differential
311 binding kinetics of **Compound 25** and derivatives with DUBs[64–67]. Note that small molecules

312 bearing electronically activated alkynes, e.g., propiolamides, for selective covalent reaction
313 with a cysteine residue of Bruton's tyrosine kinase (Btk) are in therapeutic use[68,69],
314 highlighting the potential of our USP5 inhibitor design. Structure–activity studies of
315 **Compound 25** yielded fluorinated, cell-permeable analogues **25a** and **25b**, active in cells and
316 suitable for USP5 inhibition studies. **Compound 25b** boosts type I interferon production and
317 shows potent antiviral activity, supporting known USP5 functions.

318 The combined results manifest the potential of combining cysteine-reactive, warhead-
319 containing compound sets with the *ob*ABPP-HT* workflow to streamline development of
320 selective DUB inhibitors for drug development and for use as biochemical tools in functional
321 assignment and mechanistic studies.

322 Online Methods

323 Small-molecule synthesis

324 αβ,α'β'-Diepoxyketones (DEKs) (**Compounds 1-8**) and γ-lactams (**Compounds 9-23**) were
325 synthesised as reported[26]. The synthesis of substrate-based small-molecules (**25-31 and 25a-**
326 **k**) is described in the Supplementary Information. The structures of **Compounds 1-31** are
327 shown in the Supplementary Information (Table S1-3) and the structures of **Compounds 25a-**
328 **k** are detailed in the Extended Data Table 1.

329 Cell culture

330 MCF-7 cells were cultured in high glucose DMEM supplemented with 10% fetal bovine serum
331 (FBS) (v/v) and L-glutamine (2 mM). Cells were maintained at 37 °C, 5% CO_2. MCF-7 cells were
332 washed with phosphate buffered saline (PBS) and collected in PBS by scraping and
333 centrifugation at 200 *xg* for 10 min. For data shown in Extended data Figure 1, MCF-7 cells
334 were collected by the addition of TrypLE followed by media and centrifuged at 1600 rpm for
335 5 min with pellets being resuspended in PBS (3 cycles). HAP1 cells were cultured in IMDM
336 media (#21980065) supplemented with 10% FBS (v/v), and maintained at 37 °C, 5% CO_2. ~3 ×
337 10^6 cells were seeded per 10 cm plate in 10 mL media overnight. After seeding, 4 mL of media
338 were aspirated from each plate, and recombinant human interferon-alpha, IFN-α2 (α2b; PBL
339 Assay Science; Cat. No. 11105-1), was added to the remaining media (1000 units/mL final
340 concentration). IFN-α treatment was performed for 24 h (to induce USP18), media from each

341 plate was then aspirated and cells were washed once with PBS (5 mL per plate). Cells were
342 subsequently stored at –80 °C until lysis. THP-1 cells were cultured in RPMI 1640
343 supplemented with 10% FBS (v/v), 0.05 mM β-mercaptoethanol, GlutaMAX Supplement, and
344 Penicillin-Streptomycin. Cells were maintained at 37 °C 5% CO_2. RCC4-VHL and VA cells were
345 cultured in DMEM media supplemented with 10% fetal bovine serum (FBS), GlutaMAX, and
346 Penicillin-Streptomycin[36]. Calu-3 cells were obtained from Prof Nicole Zitzmann's lab and
347 maintained in Advanced DMEM media, 10% FCS, L-glutamine, and Penicillin-Streptomycin.

348 **<u>In-depth ABPP workflows</u>**

349 **Sample preparation**

350 Cell lysis and DUB Activity-Based Enrichment: Cells were lysed in lysis buffer (50 mM Tris, pH
351 7.5, 5 mM $MgCl_2$, 0.5 mM EDTA, 1 mM DTT and 250 mM sucrose) containing acid-washed
352 glass beads (Sigma Aldrich #G4649). Glass beads made up approximately one third of the total
353 lysis buffer volume. Cell lysates were vortexed and centrifuged (14K x g, 4 °C, 25 min) to
354 separate the pellet, glass beads, nuclei, and membranes from supernatant. The supernatant
355 was transferred to Eppendorf tubes and the pellets were discarded.

356 Proteins extracted from ~$1 \cdot 10^7$ cells were used as starting materials. When profiling a DUB
357 inhibitor, PR-619 (Sigma-Aldrich # 662141) was first incubated and mixed at 1,000 rpm at 37
358 °C for 1 h. 25 µg of a DUB probe (HA-Ahx-Ahx-Ub-PA (UbiQ-078), HA-Ahx-Ahx-Ub-VME (UbiQ-
359 035), HA-Ahx-Ahx-Ub-VS (UbiQ-178)) or probe mixtures were added to each of the samples
360 and mixed at 1,000 rpm at 37 °C for 1 h. The reaction was quenched by the addition of SDS to
361 0.4% (v/v) and NP-40 to 0.5% (v/v). Lysate mixtures were then diluted to 1 mL, 0.5 mg/mL
362 with NP-40 lysis buffer (pH 7.4, 50 mM Tris, 0.5% (v/v) NP-40, 150 mM NaCl, and 20 mM
363 $MgCl_2$). 200 µL of anti-HA-Agarose (Pierce # 26182) slurry, previously washed three times with
364 NP-40 lysis buffer, was added to the samples and incubated on a rotator overnight at 4 °C.
365 After a first centrifugation step (2,000 g, 4 °C, 1 min), beads were washed four times with 500
366 µL of NP-40 lysis buffer. Protein complexes were eluted by boiling beads in 250 µL SDS
367 Laemmli 2X sample buffer.

368 Methanol-chloroform precipitation was performed prior to protease digestion. For each
369 sample, a 4x volume of methanol was added and vortexed for 5 s. A 1x volume of chloroform
370 was added to the samples, which were then vortexed for 5 s. A 3x volume of water was added,

371 and samples were vortexed for 5 s. Samples were then centrifuged for 10 min at 10,000 rpm.
372 The aqueous and organic phases were removed to leave only the protein pellet. The pellets
373 were subsequently washed with 4x volume of methanol and centrifuged for 10 min at 10,000
374 rpm. The supernatant was discarded, and pellets were re-dissolved in 100 µL of water. Protein
375 precipitation was repeated for a second time to ensure sufficient removal of detergent.

376 Sample digestion and TMT labelling were performed using the IST-NHS 96x kit (PreOmics #
377 P.O.00030) according to the manufacturer's instructions. Briefly, 100 µL lysis buffer was
378 added to each sample and heated to 95 °C while mixing at 1,000 rpm for 10 min. Lyophilised
379 digestion enzymes were dissolved in 100 µL water before being added to the samples. The
380 samples were digested at 37 °C for 2 h. For samples to be analysed by a Label-Free
381 quantitation MS method, digestion was stopped, and the sample was transferred to the
382 cartridge in a centrifuge at 2000 g for 1 min before proceeding the washing steps with wash
383 solvent 1 and 2 provided with the kit. For the remaining samples, 200 µg TMTpro 18 Plex
384 reagents (ThermoFischer Scientific # A52045) were added to each of the samples and
385 incubated for 1 h while shaking at 1000 rpm. A total of 10 µL of 5% (v/v) aqueous
386 hydroxylamine was added to each of the samples. A total of 100 µL of stop reagent was also
387 added to the samples before transferring to cartridge for washing with washing solvent 1 and
388 2 provided with the kit. Samples were eluted with 250 µL of 50% (v/v) acetonitrile in 0.01%
389 (v/v) aqueous formic acid. Samples labelled with TMT reagents were combined, dried and
390 subjected to high pH fractionation using HPLC (Agilent). Peptides were loaded into a XBridge
391 C18 column 4.6 x 250 mm (Waters # PN186003117) in buffer A (H_2O, pH 10) and eluted with
392 increasing buffer B (90% (v/v) aqueous acetonitrile, pH 10) at a 0.50 mL/min flowrate over a
393 96 min gradient. Eluted samples were collected every minute and concatenated to give a total
394 of 24 fractions. Desalting was performed by solid phase extraction (SPE) employing reversed-
395 phase C18 cartridges (Sep-Pak C18 light).

396 **LC-MS/MS methodology**

397 For LFQ Data Dependent Acquisition (DDA) and Data independent Acquisition (DIA)
398 workflows, peptides were analysed by liquid chromatography tandem mass spectrometry (LC-
399 MS/MS) using an Ultimate 3000 UHPLC coupled to an Orbitrap Fusion Lumos Mass
400 Spectrometer (both from ThermoFisher). Tryptic peptides were separated on an EASY-spray
401 PepMap column (2um, 75um x 50cm; ThermoScientific) using a 60-minute linear gradient

402 from 2 to 35% buffer B (5% DMSO, 100% acetonitrile, 0.1% TFA) with a 250nl/min flow and
403 analysed on the Orbitrap Fusion Lumos (Thermo Scientific). Data were acquired in DDA and
404 DIA as previously described[16,70,71]. In both cases the advance peak detection (ADP) was
405 enabled. For DDA, survey scans were acquired in the Orbitrap at 120 k resolution over a m/z
406 range 400 -1500, AGC target of 4e5 and S-lens RF of 30. Fragment ion spectra (MS/MS) were
407 obtained in the Ion trap (rapid scan mode) with a Quad isolation window of 1.6, 40% AGC
408 target and a maximum injection time of 35 ms, with HCD activation and 28% collision energy.
409 For DIA, MS1 scans were acquired in the Orbitrap with 120k resolution (m/z 350-1650), an
410 AGC target of 5e5 and a maximum injection time of 20ms. The full MS events were followed
411 by 40 DIA scan windows per cycle (with variable isolation width) covering the m/z range from
412 350 – 1650. The MS/M S scans were acquired in the orbitrap at 30k resolution and normalised
413 HCD set up at 30%.
414 For TMT labelled samples, mass spectrometric analyses were carried out with a Proxeon Easy
415 Nano-LC fitted with a PepMap C18 column 75 µm x 50 cm (Thermos Scientific #PN ES903) and
416 connected to a Lumos Orbitrap mass spectrometer (Thermo Scientific). Peptides were eluted
417 at 450 nL flowrate during 120 min gradient. MS data was acquired with SPS M3 approach.
418 Each full orbitrap scan (R=60K, m/z scan range: 385-1350, AGC target: 100k, max. injection
419 time: 100 ms) was acquired and followed with dependent IT MS/MS scans (isolation window:
420 0.5, CID collision energy (%): 35, AGC target: 30k ions, max. injection time: 175 ms) for a 2.7S
421 cycle time. SPS MS3 scans were acquired with the following parameters (R: 50k, isolation
422 window = 1.5, AGC target: 120k, HCD collision energy (%): 55, max. injection time: 100 ms).

423 **LC-MS/MS data analysis Single shot LFQ**

424 Data was searched using a Uniprot *Homo sapiens* database containing isoforms (42,469
425 entries, retrieved on 15/08/2023). Software versions: DIA-NN 1.8.1, Fragpipe 22.0,
426 MaxQuant/MaxDIA 2.6.1.0. All search settings were left as default, with match between runs
427 enabled and cysteine carbamidomethylation included as a fixed modification. Each search
428 was 3 x HA-Ub-* and 3 x HA-Ub-*+ 50 µM PR619. The PA warhead alone was searched
429 separately from the PA/VME/VS cocktail of warheads. The intensities output
430 'report.pg_matrix' was used from DIA-NN, the LFQ intensities from 'combined_protein'
431 output was used from Fragpipe, and the LFQ intensities from the 'protein groups' was used
432 from Maxquant for both DDA and DIA searches.

433 **LC-MS/MS data analysis TMT fractions**

434 MS data processing was performed with Proteome Discoverer Version 2.4.0.305 (Thermo
435 Scientific) with UniProtKB Swiss-Prot (TaxID = 9606, *Homo sapiens*) fasta. Peptide
436 identifications were carried out using the Sequest™ search engine with the following
437 parameters: precursor tolerance: 10 ppm, fragment tolerance = 0.6 Da, max. missed cleavage
438 sites: 3, dynamic modifications: M oxidation and N/Q deamination, fixed modifications:
439 PreOMics cysteine modification (+113.084 Da) and TMTpro (+304.207 N-terminus and K).

440 **<u>High-throughput ABPP workflows</u>**

441 **Sample preparation for Agilent Bravo ABPP high-throughput screen**

442 The data presented here on the Agilent Bravo ABPP immunoprecipitation is from published
443 work,[20] and is included for comparison.

444 **Sample preparation for *ob*ABPP-HT* ABPP high-throughput screen and compound**
445 **concentration-dependence validations**

446 HA-Ub-PA was synthesised as reported.[20,22] MCF-7 cells were washed with PBS, scraped in PBS
447 and centrifuged at 200 *g* for 10 min. Pellets were then resuspended in lysis buffer (50 mM
448 Tris, 5 mM $MgCl_2$, 0.5 mM EDTA, 250 mM sucrose, 1 mM dithiothreitol (DTT), pH 7.5), and
449 lysed using glass beads (2:1 ratio lysate to beads) with vortexing (10 cycles of 30 s vortexing
450 followed by 2 min incubation on ice). The MCF-7 lysate was then clarified at 600 *x g* for 10
451 min at 4 °C. Lysate protein concentration was determined by BCA, and 250 µg was aliquoted
452 per well, into a 96 well plate, at a concentration of ~4.7 mg/mL.

453 The compound library was diluted to 1 mM DMSO stock solutions in a 96 well plate and
454 multichannel-pipetted with mixing into the lysate plate to a final compound concentration of
455 25 µM in duplicate for the screen. For the concentration-dependence validations, the
456 indicated inhibitor concentrations were added in duplicate. Additional control wells (4 x
457 negative, 4 x positive for the screen, 3 x negative and 3 x positive for the concentration-
458 dependence validations) were treated with DMSO. The plate was then incubated at 37 °C for
459 1 h on a thermomixer and without shaking.

460 A total of 2 µg of HA-Ub-PA was multichannel-pipetted with mixing into to the positive control
461 wells and all inhibitor-treated wells, with an equivalent volume of buffer added to the

462 negative control wells. The lysates were then incubated with the HA-Ub-PA at 37 °C for 45
463 min on a thermomixer without shaking. The final reaction volume with the MCF-7 lysate,
464 inhibitor/DMSO and HA-Ub-PA/buffer was 60 µL. Reactions were quenched by the addition
465 of SDS and NP-40 (IGEPAL CA-630) to final concentrations of 0.4 % (v/v) and 0.5 % (v/v)
466 respectively. Reactions were then diluted by addition of 200 µL NP40 buffer (50 mM Tris, 0.5%
467 NP-40 (IGEPAL CA-630), 150 mM NaCl, and 20 mM $MgCl_2 \cdot 6\ H_2O$, pH 7.4).

468 75 µL of anti-HA magnetic beads were aliquoted into a separate 96 well plate and washed 5x
469 with 200 µL of NP40 buffer (50 mM Tris Base, 0.5% NP-40 (IGEPAL CA-630), 150 mM NaCl,
470 and 20 mM $MgCl_2 \cdot 6\ H_2O$, pH 7.4), using a magnetic rack for bead separation and multichannel
471 pipetting with cut tips for mixing. Reaction mixtures were then added to the washed magnetic
472 beads, mixed by multichannel-pipetting, and incubated in a thermomixer overnight at 4 °C
473 with gentle agitation (350 rpm). The beads were then washed 5x with 200 µL of NP40 buffer
474 as before.

475 Proteins were eluted from the beads and reduced by addition of 100 µL of 2 x Laemmli buffer
476 supplemented with 20 mM DTT using a multichannel pipette, and incubated for 10 min at 90
477 °C with 350 rpm on a thermomixer. Eluates were then removed from the beads using a
478 magnetic rack and transferred to a fresh 96 well plate. Eluates were alkylated by the addition
479 of iodoacetamide (IAA) to a final concentration of 40 mM. Proteins were then digested using
480 trypsin and cleaned up using a 96 well S-trap plate according to the manufacturer's
481 instructions[72], dried down in a speedvac and resuspended in 0.1% (v/v) aqueous formic acid.

482 **Sample preparation for the ABPP Thermo KingFisher Apex workflow**

483 The bio-ISG15-PA probe was synthesised as previously described[73]. Cell lysis, subsequent
484 labelling with HA-Ub-PA or bio-ISG15-PA probes, immunoprecipitation and protein
485 enrichment, and processing of samples for analysis by western blot and LC-MS/MS was
486 performed as described[74]. Briefly, HAP1 cells were treated and prepared as described in the
487 subsection '*Cell culture*'. Cells were resuspended in lysis buffer (50 mM Tris, 5 mM $MgCl_2$, 0.5
488 mM EDTA, 2.5% (v/v) glycerol, 1 mM dithiothreitol (DTT), pH 7.5), and lysed using glass beads
489 (2:1 ratio lysate to beads) with vortexing (10 x 30 s vortexing followed by 1 min incubation on
490 ice). The HAP1 lysates were then centrifuged (600 x *g* for 5 min at 4 °C; ~80% of supernatant
491 was transferred into clean tubes, then the remaining ~20% of supernatant was spinned at 14

492 000 x *g* for 10 min at 4 °C, and then the two fractions from each spin were combined). The
493 protein concentration in the lysates was estimated using the BCA assay kit (#23227), and 270
494 µg were aliquoted per well into a 96-deep well plate. The total volume in each well was made
495 up to 143 µL for samples to be labelled with HA-Ub-PA, or 147 µL for samples to be labelled
496 with bio-ISG15-PA, with lysis buffer.

497 For **Compound 3**, stock solutions (100×) were prepared at a concentration of 0.46, 1.39, 4.16
498 or 12.5 mM in DMSO in a 96-well plate, and 1.5 µL of each stock were transferred into the
499 respective wells using a multichannel pipette (resulting in a final concentration of 4.6, 13.9,
500 41.6 or 125 µM) in duplicates. Negative and probe-only positive controls were treated with
501 1.5 µL of DMSO in triplicates. The plate was then incubated at rt for 1 h without shaking.

502 Following compound incubation, 5.4 µL of HA-Ub-PA or 2.35 µL of bio-ISG15-PA (volumes
503 determined from probe titration assays for protein labelling) were transferred into the
504 respective wells using a multichannel pipette, with an equivalent volume of buffer added to
505 the corresponding negative control wells, and incubated at 37 °C for 45 min without shaking.
506 The final reaction volume with the HAP1 lysate, inhibitor or DMSO, and HA-Ub-PA or bio-
507 ISG15-PA or buffer was 150 µL. Reactions were quenched by addition of SDS and NP-40
508 (IGEPAL CA-630) to final concentrations of 0.4% (v/v) and 0.5% (v/v), respectively, from a
509 master mixture. The master mixture was prepared immediately before quenching by mixing
510 a 5% (v/v) SDS stock with a 10% (v/v) NP-40 stock in a ratio of 1.6:1 and adding 21.5 µL of the
511 mixture to each well. 20 µL of each reaction mixture was kept as 'input' samples (to evaluate
512 efficiency of probe labelling), and the remaining ~150 µL of reaction volume was diluted by
513 addition of 250 µL NP-40 buffer (50 mM Tris Base, 0.5% (v/v) NP-40 (IGEPAL CA-630), 150 mM
514 NaCl, and 20 mM $MgCl_2$, pH 7.4) to a total volume of 400 µL.

515 For immunoprecipitation/pull-down steps, 50 µL of anti-HA magnetic beads or 37.5 µL of
516 streptavidin magnetic Sepharose beads were used per sample. The appropriate total amount
517 of anti-HA magnetic beads or streptavidin magnetic Sepharose beads were split into 450 µL
518 aliquots, washed with 4 × 1.6 mL of NP-40 buffer (50 mM Tris, 0.5% NP-40 (IGEPAL CA-630),
519 150 mM NaCl, and 20 mM $MgCl_2$, pH 7.4) using a magnetic rack for bead separation, and
520 transferred into the respective reaction wells using a multichannel pipette with cut tips. The
521 96-deep well plate was then incubated for 4 h. at 4 °C on the Thermo KingFisher Apex system,
522 with mixing speed set to 'medium'. The beads were then washed with 4 × 500 µL NP-40 buffer,

523 as described above, and proteins were eluted from the beads twice with 2× Laemmli buffer
524 supplemented with 50 mM DTT (2 × 55 µL, 2 × 5 min at 95 °C with mixing speed set to 'slow').
525 Beads were removed from the eluates by programming the system to capture and release the
526 beads into an empty 96-deep well plate. Eluates were reduced with DTT to a final
527 concentration of 10 mM (15 min, rt), then alkylated by the addition of iodoacetamide (IAA)
528 to a final concentration of 20 mM (10 min, rt). Proteins were then digested using trypsin and
529 cleaned up using a 96-well S-trap plate according to the manufacturer's instructions[72], dried
530 down in a speedvac and resuspended in 0.1% (v/v) aqueous formic acid.

531 **LC-MS/MS timsTOF *ob*ABPP-HT* methodology**

532 Peptide samples were loaded onto Evotips (Evosep) desalting columns according to the
533 manufacturer's instructions, then chromatographically separated on an 8 cm x 150 µm
534 analytical column with bead size 1.5 µm (EV1109, Evosep), using an Evosep One liquid
535 chromatography (LC) system with the 100 spd standard method. Peptides were eluted onto
536 a TimsTOF Pro mass spectrometer (Bruker) operated in diaPASEF mode using 8 diaPASEF
537 scans per TIMS-MS scan. The ion mobility range was set to 0.85-1.3 Vs/cm^2. Each mass
538 window isolated was 25 m/z wide, ranging from 475-1000 m/z with an ion mobility-
539 dependent collision energy that increased linearly from 20 eV to 59 eV between 0.6-1.6
540 Vs/cm^2.

541 **LC-MS/MS for timsTOF Bravo Agilent robot methodology**

542 The previously reported timsTOF data collected after immunoprecipitation using the Agilent
543 robot sample prep methodology is identical to that detailed above[21], other than a different
544 ion mobility range (0.6–1.6 Vs/cm^2), and mass range (400–1000 m/z).

545 **LC-MS/MS for timsTOF for KingFisher Apex robot methodology**

546 Peptides were analysed by nanoLC-MS/MS using an Evosep One LC system coupled with a
547 timsTOF HT (Bruker) equipped with an 8 cm x 150 µm, 1.5 µm analytical column (Evosep). 200
548 ng peptides were separated using the Evosep 60SPD workflow (Analytical solvents A: 0.1% FA
549 and B: acetonitrile plus 0.1% FA). Column was held at 40 °C. Data were acquired in data-
550 independent acquisition PASEF mode with the following settings: m/z range from 100 m/z to
551 1700 m/z, ion mobility range from 1/K0 = 1.30 to 0.85 Vs/cm2 using equal ion accumulation

552 and ramp times in the dual TIMS analyser of 100 ms each. Each cycle consisted of 8 PASEF
553 ramps covering 21 mass steps each with 25 Da windows each with 2/3 non-overlapping ion
554 mobility windows covering the 475 to 1000 m/z range and 0.85 and 1.26 Vs/cm2 ion mobility
555 range. The collision energy was lowered as a function of increasing ion mobility from 59 eV at
556 1/K0 = 1.6 Vs/cm2 to 20 eV at 1/K0 = 0.6 Vs/cm2.

557 **ABPP-HT* *vs ob*ABPP-HT* comparison LC-MS/MS data analysis**

558 Data was searched in DIA-NN 1.8.1 with search settings left as default and match between
559 runs enabled. Data was searched using a Uniprot *Homo sapiens* database containing isoforms
560 (42,469 entries, retrieved on 15/08/2023). N=3 for HA-Ub-PA positive controls, N=1 for
561 negative controls with no HA-Ub-PA present. The 'report.pg_matrix' output was used for
562 analysis.

563 **ABPP Thermo KingFisher Apex workflow LC-MS/MS data analysis**

564 Data was searched in DIA-NN 1.8.1 with search settings left as default and match between
565 runs enabled. Data was searched using a Uniprot H*omo sapiens* database containing isoforms
566 (20412 entries, retrieved 13/12/2023). The 'report.pg_matrix' output was used (identical
567 number of DUBs were identified in the 'report.unique_genes_matrix' output). DUBs were
568 filtered to select hits >1.5-fold enriched in the positive HA-Ub-PA control *vs* the negative
569 control without HA-Ub-PA. Volcano plots were generated/calculated using GraphPad Prism
570 (Version 10.2.3). For the **Compound 3** concentration-dependence heatmap DUBs were
571 filtered for >5-fold enrichment in the positive HA-Ub-PA control *vs* the negative control
572 without HA-Ub-PA. USP6 was discounted due to it's unreliable detection across replicates.

573 ***ob*ABPP-HT* screen and concentration-dependence data analysis**

574 Data was searched in DIA-NN 1.8.1 with search settings left as default and match between
575 runs enabled. Data was searched using a Uniprot *Homo sapiens* database, not containing
576 isoforms (20,416 entries, retrieved on 15/02/2023). The 'report.unique_genes_matrix'
577 output was used to ensure inhibitor identification unique to specific DUBs. DUBs were filtered
578 to remove those that were not >5-fold enriched in the positive HA-Ub-PA control *vs* the
579 negative control without HA-Ub-PA. For the concentration-dependent data the following
580 DUBs were discounted due to their unreliable detection across replicates, likely attributable

581 to their low intensities: OTUD1, USP42, OTUD5, USP1, USP30, USP33, USP37, USP43 and
582 OTUB2. Intensities were normalised as a percentage of the positive HA-Ub-PA control and for
583 the screen multiple two-tailed unpaired (homoscedastic) T-tests were carried out (Microsoft
584 Excel) to identify DUBs with significantly different intensities relative to the positive control.
585 The resultant data were then filtered to select hits with a >20% average reduction in DUB
586 activity. The concentration-dependence ABPP outputs were processed using CurveCurator
587 (Version 0.3.0),[75] with the alpha asymptote set to 5%.

588 **ABP western blot compound validations**

589 ***ob*ABPP-HT* screen hit validations**

590 For positive hit validations by western blot the *ob*ABPP-HT* screen and Thermo KingFisher
591 Apex methodologies were used with the concentrations of compounds indicated in figures.
592 For the *ob*ABPP-HT* screen, following compound incubation and reaction with HA-Ub-PA, the
593 reaction was quenched directly with Laemmli buffer supplemented with 100 mM DTT and
594 analysed by western blot. IC_{50} values were extracted by quantifying the HA-Ub-PA labelled
595 band by densitometry (Image studio lite) normalised to the β-actin signal and subsequently
596 normalising the signal of the DUB activity to the negative and positive HA-Ub-PA controls. For
597 the Thermo KingFisher Apex workflow, following compound incubation and reaction with HA-
598 Ub-PA, the reaction was quenched directly with 2× Laemmli buffer supplemented with 50 mM
599 DTT and analysed by western blots. Concentration-dependencies were fit to
600 Y=100/(1+10^((LogIC_{50}-X)*HillSlope)) in Graphpad Prism (Version 10.1.1).

601 **Compound *vs* HA-Ub-PA time dependence competition studies**

602 Samples were processed as for the ABP western blot compound concentration-dependence
603 validations, with the HA-Ub-PA incubated for the indicated time.

604 **ABP compound cellular permeability studies**

605 MCF-7 cells were cultured in 6-well plates to 90% confluence, with a media change to 1 mL
606 prior to DMSO/compound treatment at the indicated concentration for 4 h. Cells were then
607 washed 3 x with PBS, and collected by scraping in PBS and centrifuged (200 x *g* for 10 min).
608 Pellets were then processed as outlined above in the ABPP screen sample preparation section,
609 with 0.4 µg of HA-Ub-PA being used per 50 µg of lysate protein. The mixture was incubated

610 for 45 min at 37 ˚°C, before being quenched by addition of Laemmli buffer supplemented with
611 100 mM of DTT; the mixture was then analysed by western blotting.

612 **Enzyme kinetics**

613 Fluorescence intensity measurements were used to monitor the cleavage of a ubiquitin-
614 rhodamine substrate. All activity assays were performed in black 384-well plates in assay
615 buffer (20 mM Tris, pH 8.0, 150 mM potassium glutamate, 0.1 mM TCEP and 0.03% Bovine
616 Gamma Globulin) with a final assay volume of 20 µL. USP7, 1 nM (USP7 (1-1102), DU15644,
617 MRC Protein Phosphorylation and Ubiquitylation Unit) or USP47, 10 nM (USP47 (N-terminal
618 His), DU15682, MRC Protein Phosphorylation and Ubiquitylation Unit) was added and
619 preincubated with **Compound 3** for 30 mins. 180 nM ubiquitin-rhodamine 110 (Ubiquigent)
620 was added to initiate the reaction and the fluorescence intensity was recorded for 30 mins on
621 a PherastarFSX (BMG Labtech) with an Ex_{485}/Em_{520} optic module. Initial rates were plotted
622 against compound concentration to determine IC_{50}. To investigate the time-dependence of
623 the potency of **Compound 3**, activity assays were repeated without a preincubation step.

624 **HDX-MS**

625 **Sample Preparation**

626 Hydrogen Deuterium eXchange Mass Spectrometry (HDX-MS) experiments were performed
627 on the same stock of recombinant USP7 and USP47 protein constructs as those used in the *in*
628 *vitro* enzyme kinetics experiments. USP7 was provided at a concentration of 25.3 µM and
629 USP47 at 16.5 µM, respectively. Both proteins were prepared in 50 mM HEPES, pH 7.5, 10%
630 glycerol, 150 mM NaCl, 1 mM DTT. The initial stock concentration of **Compound 3** was 30 mM
631 in DMSO. In solution HDX-MS was performed by preparing a volume-to-volume mixture at a
632 molar ratio of 1:2 of protein:**Compound 3** (*i.e.*, the holo-state). Samples were diluted to
633 achieve a final concentration of 16 pmol on column per reaction for USP7 and 21 pmol on
634 column per reaction for USP47. Equivalent control samples (*i.e.*, the apo-state) were prepared
635 where DMSO was supplemented in place of the compound.

636 **Data Acquisition**

637 HDX-MS was performed as previously described[76]. Briefly, an identical labeling buffer was
638 prepared as that of the protein stocks except in deuterium oxide D_2O (99+ %D, Cambridge

639 Isotope Laboratories, Tewksbury, MA) and with the 10% glycerol was removed (a final
640 composition of 50 mM HEPES, pH 7.5, 150 mM NaCl, 1 mM DTT). The pH of the labeling buffer
641 was measured and corrected to pD (pD=pH+0.4). The quenching buffer comprised of 2M
642 Guanidine HCl, 100 mM citric acid, pH 2.3 in H_2O. Proteins +/- **Compound 3** were preincubated
643 for 30 min at room temperature to allow complexes to form. Samples were then diluted with
644 the labeling buffer in a 1:20 ratio, achieving an excess D_2O concentration of 95%). Several
645 labeling time points were sampled at 20 °C, more specifically, at 30, 600, and 3600 s). All
646 analyses were acquired in triplicate. Non-deuterated controls were prepared in an identical
647 fashion, with H_2O in place of D_2O. At the end of each labeling time point, samples were
648 quenched upon addition of quench buffer (1:1 ratio), resulting in a final pH of 2.5. Samples
649 were subsequently digested with a dual pepsin/proteaseXIII column (2.1 x 3.0 mm;
650 NovaBioAssays, MA) at 8 °C for 3 min. Peptides were trapped on a 1.0 mm x 5.0 mm, 5.0 µm
651 trap cartridge (Thermo Scientific™ Acclaim PepMap100) for desalting. The flow rate was
652 maintained at 150 µL/min. Peptides were then separated on a Thermo Scientific™ Hypersil
653 Gold™, 50 x 1 mm, 1.9 um, C18 column increasing hydrophobicity achieved by a linear gradient
654 of 10% to 40% Buffer B (A: water, 0.1% FA; B: ACN, 0.1% FA). The flow rate was maintained at
655 40 µL/min. A protease wash (2M guanidine, 100 mM citric acid, pH 2.3 in H_2O) was performed
656 for each run to limit carry-over. To minimise back-exchange, the quenching, trapping, and
657 separation steps were performed at 1.5°C. Labeling, quenching, and online digestion steps
658 were performed with the aid of an automated HDX robot (Trajan Scientific and Medical).
659 Sample preparation was managed in Chronos (version 5.4.1). All samples were acquired in
660 MS1 mode on Thermo Scientific™ Orbitrap Exploris™ 480 Hybrid™ mass spectrometer.

661 **Data Analysis**

662 Before each HDX-MS experiment, an unspecific digested peptide database was created in
663 BioPharma Finder (version 5.2) for non-deuterated USP7 and USP47 proteins through a data-
664 dependent and targeted HCD-MS^2 acquisition regime[76]. Labeling data were processed and
665 manually curated in HDExaminer version 3.4.2 (Trajan Scientific and Medical). The charge
666 state with the highest quality spectra for all replicates for each peptide across all HDX-MS
667 labeling times was used in the final analysis. The significant differences observed at each
668 residue was used to map HDX-MS consensus effects (based on overlapping peptides) onto the
669 AlphaFold model.

670 **Caspase-1 assay**

671 PMA-differentiated THP-1 cells were treated as indicated, and the caspase-1 activity in the
672 culture medium (supernatant) was measured using the Caspase-Glo 1 Inflammasome Assay
673 (Promega) according to the manufacturer's instruction. Briefly, the Caspase-Glo 1 Reagent
674 was prepared by resuspending the Z-WEHD substrate in Caspase-Glo 1 buffer and addition of
675 MG132 inhibitor to a final concentration of 60 µM. Cell culture medium (50 µL) was then
676 added to the Caspase-Glo 1 Reagent (50 µL) in a 96-well plate and the resultant mixture was
677 incubated at room temperature for 1 h. Luminescence was measured using a FLUOstar
678 Omega multi-mode microplate reader (BMG LABTECH) according to the manufacturer's
679 instructions.

680 **MTS cell viability assay**

681 Cell viability was assessed using the CellTiter 96 AQueous One Solution Cell Proliferation Assay
682 (MTS, Promega). The One Solution Reagent (20 µL) was added to each well of a 96-well plate
683 containing 100 µL of sample in culture medium. Following incubation at 37 °C for 1 h,
684 absorbance was measured at the wavelength of 490 nm using a FLUOstar Omega multi-mode
685 microplate reader (BMG LABTECH). Cell viability was calculated according to the
686 manufacturer's instruction.

687 **ASC speck oligomer crosslinking**

688 ASC oligomer chemical crosslinking was performed as previously described[70]. Briefly, PMA-
689 differentiated THP-1 cells were primed with LPS (1 µg/mL) for 4 h, followed by stimulation
690 with nigericin (10 µM) for 45 min and indicated concentrations of **Compound 3**. Cells were
691 lysed on ice in Buffer A (20 mM HEPES, pH 7.5, 10 mM KCl, 1.5 mM $MgCl_2$, 1 mM EDTA, 1 mM
692 EGTA, 320 mM sucrose, and protease inhibitors), and homogenised using a 21-gauge needle.
693 Lysates were centrifuged at 300 × g for 8 min at 4 °C. The supernatants were collected, mixed
694 1:1 with CHAPS buffer (20 mM HEPES, pH 7.5, 5 mM $MgCl_2$, 0.5 mM EGTA, 0.1% CHAPS, and
695 protease inhibitors), and centrifuged at 2,400 × g for 8 min to pellet crude inflammasome
696 complexes. Pellets were washed twice with ice-cold PBS, resuspended in CHAPS buffer, and
697 cross-linked with 2 mM DSS (prepared in DMSO) at 37 °C for 20 min. The reaction was
698 quenched with NuPAGE™ LDS Sample Buffer (4X) and subjected to Western blot analysis.

699 **Alignment and structure prediction of *homo sapiens* and Pan *troglodytes* USP47**

700

701 For kinetic and HDX MS studies of **Compound 3**, full-length *Homo Sapiens* USP7 and full-length
702 *Pan troglodytes* isoform 2 were used. Sequences of full-length *Homo sapiens* canonical USP47
703 and full-length USP47 from *Pan troglodytes* isoform 2 were aligned using T-coffee multiple
704 sequence alignment with differences reported at Extended Data Fig. 8a[77]. The sequences,
705 including the His-tag of the recombinant *Pan troglodytes* isoform 2, were then used to predict
706 the structures using AlphaFold 3[78], with the highest-ranking structures being superposed
707 using PyMOL (version 2.5.0) with an RMSD of 2.511 (Extended Data Fig. 8b and 8c).

708 **HIF-1α hypoxia conditions and Covid-19 infection assay**

709 SARS-CoV-2 Australia/VIC01/2020 virus and cells were provided by the Peter Doherty
710 Institute for Infection and Immunity, Melbourne, Australia at P1 and passaged twice in
711 Vero/hSLAM cells (Cat#04091501) - obtained from the European Collection of Cell Cultures
712 (ECACC), UK. Virus infectivity was determined by plaque assay on Vero-TMPRSS2 cells as
713 previously reported[79]. Calu-3 cells were infected with the above strain of SARS-CoV-2 at an
714 MOI of 0.01 for 2 h. Viral inocula were removed, cells washed three times in PBS and
715 maintained in growth media until harvest. Cell lines were maintained at 37 °C and 5% CO_2 in
716 a standard culture incubator and exposed to hypoxia using an atmosphere-regulated
717 workstation set to 37 °C, 5% CO_2:1%–5% O_2:balance N_2 (Invivo$_2$ 200, Baker-Ruskinn
718 Technologies). For quantification of viral RNA, total cellular RNA was extracted using the
719 RNeasy kit (Qiagen) according to manufacturer's instructions. Equal amounts of RNA, as
720 determined by Nanodrop analysis, were used in a one-step RT-qPCR using the Takyon-One
721 Step RT probe mastermix (Eurogentec) and run on a Roche Light Cycler 96. For quantification
722 of viral copy numbers, qPCR runs contained serial dilutions of viral RNA standards. Total SARS-
723 CoV-2 RNA was quantified using: 2019-nCoV_N1-F: 5'-GAC CCC AAA ATC AGC GAA AT-3',
724 2019-nCoV_N1-R: 5'-TCT GGT TAC TGC CAG TTG AA TCT G-3', 2019nCoV_N1-Probe: 5'-FAM-
725 ACC CCG CAT TAC GTT TGG TGG ACC-BHQ1-3'. For assaying the antiviral response against
726 **Compound 25b**, Calu-3 cells were infected with a SARS-CoV-2 reporter virus containing a
727 mNeonGreen fluorescent reporter as previously described at a MOI of 0.1[80]. Infected cells
728 were treated with serial dilutions of the compound for 24 h followed by fixation in 4% PFA.
729 Cells were stained with DAPI and mNeonGreen fluorescence was quantified by Clariostar.

730 Fluorescence data was normalised to the DAPI signal and plotted as relative to the DMSO
731 control.

732 **Type I interferon production**

733 Type I interferon production was performed as previously described[81], using HEK293 cells
734 transduced with a pGreenFire-ISRE reporter. In brief, HAP1 cells were seeded at 5,000 cells
735 per well in a 96-well plate in DMEM containing 10% FBS and 2 mM glutamine. After
736 attachment, cells were treated with **Compound 25b** for 1 h, followed by poly(I:C) (0.5mg/mL)
737 for 48 h. HAP1 media was then collected, centrifuged, and transferred to HEK293 IFN reporter
738 cells, which were seeded at 25,000 cells per well in a 96-well plate and allowed to attach.
739 Recombinant human IFNα2 (PBL assay science) was used for standards. After 24 h, the One-
740 Glo Luciferase Assay System (Promega) was used to quantify luciferase expression following
741 manufacturer's instructions.

742 **Cell growth and proliferation assays**

743 A total of 5,000 cells were seeded into either 6-well or 12-well plates and imaged using an
744 IncuCyte Zoom Imager (Sartorius) for live-cell imaging. Imaging was performed at the
745 specified time points using the phase-contrast channel, as previously described[73]. Cell growth
746 was assessed by measuring the percentage confluence.

747 **Molecular docking**

748 A model for human USP47 catalytic domain (UniProt: Q96K76), which is representative of a
749 covalently bound inhibitor conformational state, was generated using the structure of human
750 USP7 in complex with the covalent inhibitor, FT827 (PDB: 5NGF; Turnbull *et al*., 2017), as the
751 template in SwissModel[82]. Coordinates for **Compound 3** were generated using ChemDraw
752 Prime 23.0.1.10 and molecular docking was performed using CovDock[83] implemented in
753 Maestro version 13.8.135 (Schrödinger Release 2024-3: Maestro, Schrödinger, LLC, New York,
754 NY, 2024). The best docking pose for **Compound 3** corresponded to a docking score of -5.704.

755 **Antibodies**

List of antibodies used for immunoblotting in this study:

Reagent	Brand	Catalogue Number	Notes
USP5	Proteintech	10473-1-AP	
USP7	ENZO	BML-PW0540-0100	
USP18 (D4E7)	Cell Signaling Technology	4813	
USP30	Atlas antibodies	HPA016952	
USP33	Proteintech	20445-1-AP	
USP47	Abcam	ab72143	
OTUD7B	Cell Signaling Technology	14817	
VCPIP1	Cell Signaling Technology	88153	
HA (12CA5)	Roche	11666606001	
CFL1	Cell Signaling Technology	5175	
NLRP3(D4D8T)	Cell Signaling Technology	15101	
Caspase-1(D7F10)	Cell Signaling Technology	3866	
ASC(B-3)	Santa Cruz	sc-514414	
IL-1b(D3U3E)	Cell Signaling Technology	12703	
Cleaved-IL-1b (Asp116) (D3A3Z)	Cell Signaling Technology	83186	
GSDMD	Novus Biologicals	NBP2-33422	
HIF-1α	BD Biosciences	610959	
β-actin	Sigma Aldrich	A5441	Used in Fig. 2, 3, 5b, 5c-e, and Extended Data Fig. 2, 4.
β-actin (8H10D10)	Cell Signaling Technology	3700	Used in Extended Data Fig. 3f.
IRDye 680RD Streptavidin	Li-Cor	926-68079	Used for Biotinylated protein detection in Extended Data Fig. 3f.

Data availability

The mass spectrometry proteomics data have been deposited to the ProteomeXchange Consortium via the PRIDE partner repository with the dataset identifier PXD064209. The mass spectrometry HDX data have been deposited to the ProteomeXchange Consortium via the PRIDE partner repository with the dataset identifier PXD064060.

References

1. Schauer, N. J., Magin, R. S., Liu, X., Doherty, L. M. & Buhrlage, S. J. Advances in Discovering Deubiquitinating Enzyme (DUB) Inhibitors. *J Med Chem* **63**, 2731–2750 (2020).

2. Fang, T. S. Z. *et al.* Knockout or inhibition of USP30 protects dopaminergic neurons in a Parkinson's disease mouse model. *Nature Communications 2023 14:1* **14**, 1–16 (2023).

3. Okarmus, J. *et al.* USP30 inhibition induces mitophagy and reduces oxidative stress in parkin-deficient human neurons. *Cell Death & Disease 2024 15:1* **15**, 1–13 (2024).

770 4. Damgaard, R. B. The ubiquitin system: from cell signalling to disease biology and new
771 therapeutic opportunities. *Cell Death & Differentiation 2021 28:2* **28**, 423–426 (2021).

772 5. Lange, S. M., Armstrong, L. A. & Kulathu, Y. Deubiquitinases: From mechanisms to their
773 inhibition by small molecules. *Mol Cell* **82**, 15–29 (2022).

774 6. Harrigan, J. A., Jacq, X., Martin, N. M. & Jackson, S. P. Deubiquitylating enzymes and drug
775 discovery: emerging opportunities. *Nat Rev Drug Discov* **17**, 57–78 (2018).

776 7. Cadzow, L. *et al.* KSQ-4279, a first-in-class USP1 inhibitor shows strong combination activity in
777 BRCA mutant cancers with intrinsic or acquired resistance to PARP inhibitors. *Eur J Cancer*
778 **174**, S37–S38 (2022).

779 8. Yap, T. A. *et al.* First-in-human phase I trial of the oral first-in-class ubiquitin specific
780 peptidase 1 (USP1) inhibitor KSQ-4279 (KSQi), given as single agent (SA) and in combination
781 with olaparib (OLA) or carboplatin (CARBO) in patients (pts) with advanced solid tumors,
782 enriched for deleterious homologous recombination repair (HRR) mutations. *Journal of*
783 *Clinical Oncology* **42**, 3005–3005 (2024).

784 9. Bedford, D. *et al.* P0514USP30 INHIBITOR ATTENUATES PROGRESSIVE FIBROSIS IN ISCHEMIA
785 INDUCED CHRONIC KIDNEY DISEASE (CKD), EVEN AFTER DELAYED TREATMENT INITIATION
786 AFTER INJURY. *Nephrology Dialysis Transplantation* **35**, (2020).

787 10. Mondal, M., Cao, F., Conole, D., Auner, H. W. & Tate, E. W. Discovery of potent and selective
788 activity-based probes (ABPs) for the deubiquitinating enzyme USP30. *RSC Chem Biol* **5**, 439–
789 446 (2024).

790 11. Love, K. R., Pandya, R. K., Spooner, E. & Ploegh, H. L. Ubiquitin C-terminal electrophiles are
791 activity-based probes for identification and mechanistic study of ubiquitin conjugating
792 machinery. *ACS Chem Biol* **4**, 275–287 (2009).

793 12. Conole, D., Mondal, M., Majmudar, J. D. & Tate, E. W. Recent Developments in Cell
794 Permeable Deubiquitinating Enzyme Activity-Based Probes. *Front Chem* **7**, 508897 (2019).

795 13. Borodovsky, A. *et al.* Chemistry-based functional proteomics reveals novel members of the
796 deubiquitinating enzyme family. *Chem Biol* **9**, 1149–1159 (2002).

797 14. Ekkebus, R. *et al.* On Terminal Alkynes That Can React with Active-Site Cysteine Nucleophiles
798 in Proteases. *J Am Chem Soc* **135**, 2867–2870 (2013).

799 15. Josue Ruiz, E. *et al.* Usp28 deletion and small-molecule inhibition destabilizes c-myc and
800 elicits regression of squamous cell lung carcinoma. *Elife* **10**, (2021).

801 16. O'Brien, D. P. *et al.* Structural Premise of Selective Deubiquitinase USP30 Inhibition by Small-
802 Molecule Benzosulfonamides. *Mol Cell Proteomics* **22**, 100609 (2023).

803 17. Imhoff, R. D. *et al.* Covalent Fragment Screening and Optimization Identifies the
804 Chloroacetohydrazide Scaffold as Inhibitors for Ubiquitin C-terminal Hydrolase L1. *J Med*
805 *Chem* **67**, 4496–4524 (2024).

806 18. Chan, W. C. *et al.* Accelerating inhibitor discovery for deubiquitinating enzymes. *Nature*
807 *Communications 2023 14:1* **14**, 1–13 (2023).

808 19. Niphakis, M. J. & Cravatt, B. F. Ligand discovery by activity-based protein profiling. *Cell Chem*
809 *Biol* **31**, 1636–1651 (2024).

810 20. Jones, H. B. L., Heilig, R., Fischer, R., Kessler, B. M. & Pinto-Fernández, A. ABPP-HT - High-
811 Throughput Activity-Based Profiling of Deubiquitylating Enzyme Inhibitors in a Cellular
812 Context. *Front Chem* **9**, 44 (2021).

813 21. Jones, H. B. L. *et al.* ABPP-HT*—Deep Meets Fast for Activity-Based Profiling of
814 Deubiquitylating Enzymes Using Advanced DIA Mass Spectrometry Methods. *Int J Mol Sci* **23**,
815 3263 (2022).

816 22. Pinto-Fernández, A. *et al.* Comprehensive Landscape of Active Deubiquitinating Enzymes
817 Profiled by Advanced Chemoproteomics. *Front Chem* **7**, 592 (2019).

818 23. Gan, J. *et al.* USP16 is an ISG15 cross-reactive deubiquitinase that targets pro-ISG15 and
819 ISGylated proteins involved in metabolism. *Proceedings of the National Academy of Sciences*
820 **120**, e2315163120 (2023).

821 24. Mukhopadhyay, R. *et al.* USP24 is an ISG15 cross-reactive deubiquitinase that mediates IFN-I
822 production by de-ISGylating the RNA helicase MOV10. *bioRxiv* 2024.09.06.611391 Preprint at
823 https://doi.org/10.1101/2024.09.06.611391 (2024).

824 25. O'Dea, R. *et al.* Molecular basis for ubiquitin/Fubi cross-reactivity in USP16 and USP36. *Nat*
825 *Chem Biol* **19**, 1394–1405 (2023).

826 26. de Munnik, M. *et al.* αβ,α'β'-Diepoxyketones are mechanism-based inhibitors of nucleophilic
827 cysteine enzymes. *Chemical Communications* **59**, 12859–12862 (2023).

828 27. Gayatri *et al.* Thiophene-fused γ-lactams inhibit the SARS-CoV-2 main protease via reversible
829 covalent acylation. *Chem Sci* **15**, 7667–7678 (2024).

830 28. Turnbull, A. P. *et al.* Molecular basis of USP7 inhibition by selective small-molecule inhibitors.
831 *Nature 2017 550:7677* **550**, 481–486 (2017).

832 29. Catic, A. *et al.* Screen for ISG15-crossreactive Deubiquitinases. *PLoS One* **2**, e679 (2007).

833 30. Altun, M. *et al.* Activity-Based Chemical Proteomics Accelerates Inhibitor Development for
834 Deubiquitylating Enzymes. *Chem Biol* **18**, 1401–1412 (2011).

835 31. Weinstock, J. *et al.* Selective Dual Inhibitors of the Cancer-Related Deubiquitylating Proteases
836 USP7 and USP47. *ACS Med Chem Lett* **3**, 789–792 (2012).

837 32. Palazón-Riquelme, P. *et al.* USP7 and USP47 deubiquitinases regulate NLRP3 inflammasome
838 activation. *EMBO Rep* **19**, (2018).

839 33. Shin, S. C. *et al.* Structural and functional characterization of USP47 reveals a hot spot for
840 inhibitor design. *Commun Biol* **6**, 970 (2023).

841 34. Rougé, L. *et al.* Molecular Understanding of USP7 Substrate Recognition and C-Terminal
842 Activation. *Structure* **24**, 1335–1345 (2016).

843 35. Bremm, A., Moniz, S., Mader, J., Rocha, S. & Komander, D. Cezanne (OTUD 7B) regulates HIF -
844 1α homeostasis in a proteasome-independent manner . *EMBO Rep* **15**, 1268–1277 (2014).

845 36. Hu, C.-J., Wang, L.-Y., Chodosh, L. A., Keith, B. & Simon, M. C. Differential Roles of Hypoxia-
846 Inducible Factor 1α (HIF-1α) and HIF-2α in Hypoxic Gene Regulation. *Mol Cell Biol* **23**, 9361–
847 9374 (2003).

848 37. Wing, P. A. C. *et al.* Hypoxic and pharmacological activation of HIF inhibits SARS-CoV-2
849 infection of lung epithelial cells. *Cell Rep* **35**, 109020 (2021).

850 38. Qiao, Z. *et al.* USP5 inhibits anti-RNA viral innate immunity by deconjugating K48-linked
851 unanchored and K63-linked anchored ubiquitin on IRF3. *PLoS Pathog* **21**, e1012843 (2025).

852 39. Liu, Q. *et al.* Broad and diverse mechanisms used by deubiquitinase family members in
853 regulating the type I interferon signaling pathway during antiviral responses. *Sci Adv* **4**,
854 (2018).

855 40. Ge, F. *et al.* Deubiquitinating enzymes: Promising targets for drug resistance. *Drug Discov*
856 *Today* **27**, 2603–2613 (2022).

857 41. Liu, P., Chen, Z., Guo, Y., He, Q. & Pan, C. Recent advances in small molecule inhibitors of
858 deubiquitinating enzymes. *Eur J Med Chem* **287**, 117324 (2025).

859 42. Varca, A. C. *et al.* Identification and validation of selective deubiquitinase inhibitors. *Cell*
860 *Chem Biol* **28**, 1758-1771.e13 (2021).

861 43. Wallach, I. *et al.* AI is a viable alternative to high throughput screening: a 318-target study. *Sci*
862 *Rep* **14**, 7526 (2024).

863 44. Niphakis, M. J. & Cravatt, B. F. Enzyme Inhibitor Discovery by Activity-Based Protein Profiling.
864 *Annu Rev Biochem* **83**, 341–377 (2014).

865 45. Henning, N. J. *et al.* Deubiquitinase-targeting chimeras for targeted protein stabilization. *Nat*
866 *Chem Biol* **18**, 412–421 (2022).

867 46. Backus, K. M. *et al.* Proteome-wide covalent ligand discovery in native biological systems.
868 *Nature* **534**, 570–574 (2016).

869 47. Nomura, D. K., Dix, M. M. & Cravatt, B. F. Activity-based protein profiling for biochemical
870 pathway discovery in cancer. *Nat Rev Cancer* **10**, 630–638 (2010).

871 48. Vuorinen, A. *et al.* Enantioselective OTUD7B fragment discovery through chemoproteomics
872 screening and high-throughput optimisation. *Commun Chem* **8**, 12 (2025).

873 49. Cho, J. *et al.* USP47 Promotes Tumorigenesis by Negative Regulation of p53 through
874 Deubiquitinating Ribosomal Protein S2. *Cancers (Basel)* **12**, 1137 (2020).

875 50. Lei, H. *et al.* Targeting USP47 overcomes tyrosine kinase inhibitor resistance and eradicates
876 leukemia stem/progenitor cells in chronic myelogenous leukemia. *Nat Commun* **12**, 51
877 (2021).

878 51. Pan, K., Fu, J. & Xu, W. Role of Ubiquitin-Specific Peptidase 47 in Cancers and Other Diseases.
879 *Front Cell Dev Biol* **9**, (2021).

880 52. Zhai, W. & Jin, Y. OTUD7B: A potential therapeutic target in the treatment of gastric cancer?
881 *Digestive and Liver Disease* **56**, 536 (2024).

882 53. Tang, J., Wu, Z., Tian, Z., Chen, W. & Wu, G. OTUD7B stabilizes estrogen receptor α and
883 promotes breast cancer cell proliferation. *Cell Death Dis* **12**, 534 (2021).

884 54. Pareja, F. *et al.* Deubiquitination of EGFR by Cezanne-1 contributes to cancer progression.
885 *Oncogene* **31**, 4599–4608 (2012).

886 55. Lin, D. *et al.* Upregulation of OTUD7B (Cezanne) Promotes Tumor Progression via AKT/VEGF
887 Pathway in Lung Squamous Carcinoma and Adenocarcinoma. *Front Oncol* **9**, (2019).

888 56. Chen, J. *et al.* AtomNet-Aided OTUD7B Inhibitor Discovery and Validation. *Cancers (Basel)* **15**,
889 517 (2023).

890 57. Wing, P. A. C. *et al.* Hypoxia inducible factors regulate infectious SARS-CoV-2, epithelial
891 damage and respiratory symptoms in a hamster COVID-19 model. *PLoS Pathog* **18**, e1010807
892 (2022).

893 58. Reyes-Turcu, F. E. *et al.* The Ubiquitin Binding Domain ZnF UBP Recognizes the C-Terminal
894 Diglycine Motif of Unanchored Ubiquitin. *Cell* **124**, 1197–1208 (2006).

895 59. Gao, S.-T., Xin, X., Wang, Z., Hu, Y. & Feng, Q. USP5: Comprehensive insights into structure,
896 function, biological and disease-related implications, and emerging therapeutic
897 opportunities. *Mol Cell Probes* **73**, 101944 (2024).

898 60. Mann, M. K. *et al.* Structure–Activity Relationship of USP5 Inhibitors. *J Med Chem* **64**, 15017–
899 15036 (2021).

900 61. Mann, M. K. *et al.* Discovery of Small Molecule Antagonists of the USP5 Zinc Finger Ubiquitin-
901 Binding Domain. *J Med Chem* **62**, 10144–10155 (2019).

902 62. Bonnet, J., Romier, C., Tora, L. & Devys, D. Zinc-finger UBPs: regulators of deubiquitylation.
903 *Trends Biochem Sci* **33**, 369–375 (2008).

904 63. Covalent Ubiquitin-Usp5 Complex. Preprint at https://doi.org/10.2210/pdb3ihp/pdb (2009).

905 64. Mons, E. *et al.* The Alkyne Moiety as a Latent Electrophile in Irreversible Covalent Small
906 Molecule Inhibitors of Cathepsin K. *J Am Chem Soc* **141**, 3507–3514 (2019).

907 65. Brewitz, L. *et al.* Alkyne Derivatives of SARS-CoV-2 Main Protease Inhibitors Including
908 Nirmatrelvir Inhibit by Reacting Covalently with the Nucleophilic Cysteine. *J Med Chem* **66**,
909 2663–2680 (2023).

910 66. Krummenacher, D. *et al.* Discovery of Orally Available and Brain Penetrant AEP Inhibitors. *J*
911 *Med Chem* **66**, 17026–17043 (2023).

912 67. Laczi, D. *et al.* Silaproline-bearing nirmatrelvir derivatives are potent inhibitors of the SARS-
913 CoV-2 main protease highlighting the value of silicon-derivatives in structure-activity-
914 relationship studies. *Eur J Med Chem* **291**, 117603 (2025).

915 68. Barf, T. *et al.* Acalabrutinib (ACP-196): A Covalent Bruton Tyrosine Kinase Inhibitor with a
916 Differentiated Selectivity and In Vivo Potency Profile. *J Pharmacol Exp Ther* **363**, 240–252
917 (2017).

918 69. Liclican, A. *et al.* Biochemical characterization of tirabrutinib and other irreversible inhibitors
919 of Bruton's tyrosine kinase reveals differences in on - and off - target inhibition. *Biochimica et*
920 *Biophysica Acta (BBA) - General Subjects* **1864**, 129531 (2020).

921 70. Liang, Z. *et al.* Proximity proteomics reveals UCH-L1 as an essential regulator of NLRP3-
922 mediated IL-1β production in human macrophages and microglia. *Cell Rep* **43**, 114152 (2024).

923 71. Muntel, J. *et al.* Comparison of Protein Quantification in a Complex Background by DIA and
924 TMT Workflows with Fixed Instrument Time. *J Proteome Res* **18**, 1340–1351 (2019).

925 72. HaileMariam, M. *et al.* S-Trap, an Ultrafast Sample-Preparation Approach for Shotgun
926 Proteomics. *J Proteome Res* **17**, 2917–2924 (2018).

927 73. Pinto-Fernandez, A. *et al.* Deletion of the deISGylating enzyme USP18 enhances tumour cell
928 antigenicity and radiosensitivity. *Br J Cancer* **124**, 817–830 (2021).

929 74. Jones, H. B. L., Heilig, R., Kessler, B. M. & Pinto-Fernández, A. Activity-Based Protein Profiling
930 (ABPP) for Cellular Deubiquitinase (DUB) and Inhibitor Profiling at Deep and High-Throughput
931 Levels. *Methods in Molecular Biology* **2591**, 101–122 (2023).

932 75. Bayer, F. P., Gander, M., Kuster, B. & The, M. CurveCurator: a recalibrated F-statistic to
933 assess, classify, and explore significance of dose–response curves. *Nat Commun* **14**, 7902
934 (2023).

935 76. O'Brien, D. P. *et al.* Structural Dynamics of the Ubiquitin Specific Protease USP30 in Complex
936 with a Cyanopyrrolidine-Containing Covalent Inhibitor. *J Proteome Res* **24**, 479–490 (2025).

937 77. Notredame, C., Higgins, D. G. & Heringa, J. T-coffee: a novel method for fast and accurate
938 multiple sequence alignment 1 1Edited by J. Thornton. *J Mol Biol* **302**, 205–217 (2000).

939 78. Abramson, J. *et al.* Accurate structure prediction of biomolecular interactions with AlphaFold
940 3. *Nature* **630**, 493–500 (2024).

941 79. Puray-Chavez, M. *et al.* Systematic analysis of SARS-CoV-2 infection of an ACE2-negative
942 human airway cell. *Cell Rep* **36**, 109364 (2021).

943 80. Erdmann, M. *et al.* Development of SARS-CoV-2 replicons for the ancestral virus and variant
944 of concern Delta for antiviral screening. Preprint at
945 https://doi.org/10.1101/2022.10.11.511804 (2022).

946 81. Bridgeman, A. *et al.* Viruses transfer the antiviral second messenger cGAMP between cells.
947 *Science (1979)* **349**, 1228–1232 (2015).

948 82. Waterhouse, A. *et al.* SWISS-MODEL: homology modelling of protein structures and
949 complexes. *Nucleic Acids Res* **46**, W296–W303 (2018).

950 83. Zhu, K. *et al.* Docking Covalent Inhibitors: A Parameter Free Approach To Pose Prediction and
951 Scoring. *J Chem Inf Model* **54**, 1932–1940 (2014).

952 84. Madeira, F. *et al.* The EMBL-EBI Job Dispatcher sequence analysis tools framework in 2024.
953 *Nucleic Acids Res* **52**, W521–W525 (2024).

954 85. Letunic, I. & Bork, P. Interactive Tree of Life (iTOL) v6: recent updates to the phylogenetic tree
955 display and annotation tool. *Nucleic Acids Res* **52**, W78–W82 (2024).

956 86. Erdmann, M. *et al.* A Novel Toolkit of SARS-CoV-2 Sub-Genomic Replicons for Efficient
957 Antiviral Screening. *Viruses* **17**, 597 (2025).

87. Hu, M. *et al.* Crystal Structure of a UBP-Family Deubiquitinating Enzyme in Isolation and in Complex with Ubiquitin Aldehyde. *Cell* **111**, 1041–1054 (2002).

Acknowledgements

The A.P.-F. and B.M.K. labs were supported by the Chinese Academy of Medical Sciences Innovation Fund for Medical Science, China (grant number: 2018-I2M-2-002) and by Pfizer Inc. The A.P.-F. lab was also supported by CRUK, Ono Pharma, and Boehringer Ingelheim. We would like to thank Prof. Jan Rehwinkel for the type I interferon reporter cells. H.B.L.J. was supported by a Bristol-Myers Squibb fellowship.

Author contributions

H.B.L.J., S.D., L.B., and A.P.-F. designed research; H.B.L.J., S.D., S.S.H., P.A.C.W., C.N., Z.L., J.D., J.L., E.M., A.B., A.P., J.W.H., M.E.R., S.F., A.T., D.O.B., E.S., and A.P.T. performed research; P.R.E. contributed new reagents/analytic tools; I.V., E.W.T., D.O.B., G.M.W., B.M.K., C.J.S., L.B., A.P.-F. provided supervison; H.B.L.J., L.B., and A.P.-F. wrote the paper, and D.O.B., S.D., S.S.H., A.P.T., C.J.S., P.R.E., and B.M.K. provided feedback on the manuscript.

Ethics declaration

Non applicable

Competing interests

The authors declare that they have no competing interests affecting the contents of this article.

Corresponding authors

Hannah B.L. Jones (H.B.L.J.), Lennart Brewitz (L.B.), and Adán Pinto-Fernández (A.P.-F.)

Figures

Fig. 1 High-throughput and sensitive DUB activity proteomics methodology: *ob*ABPP-HT*.

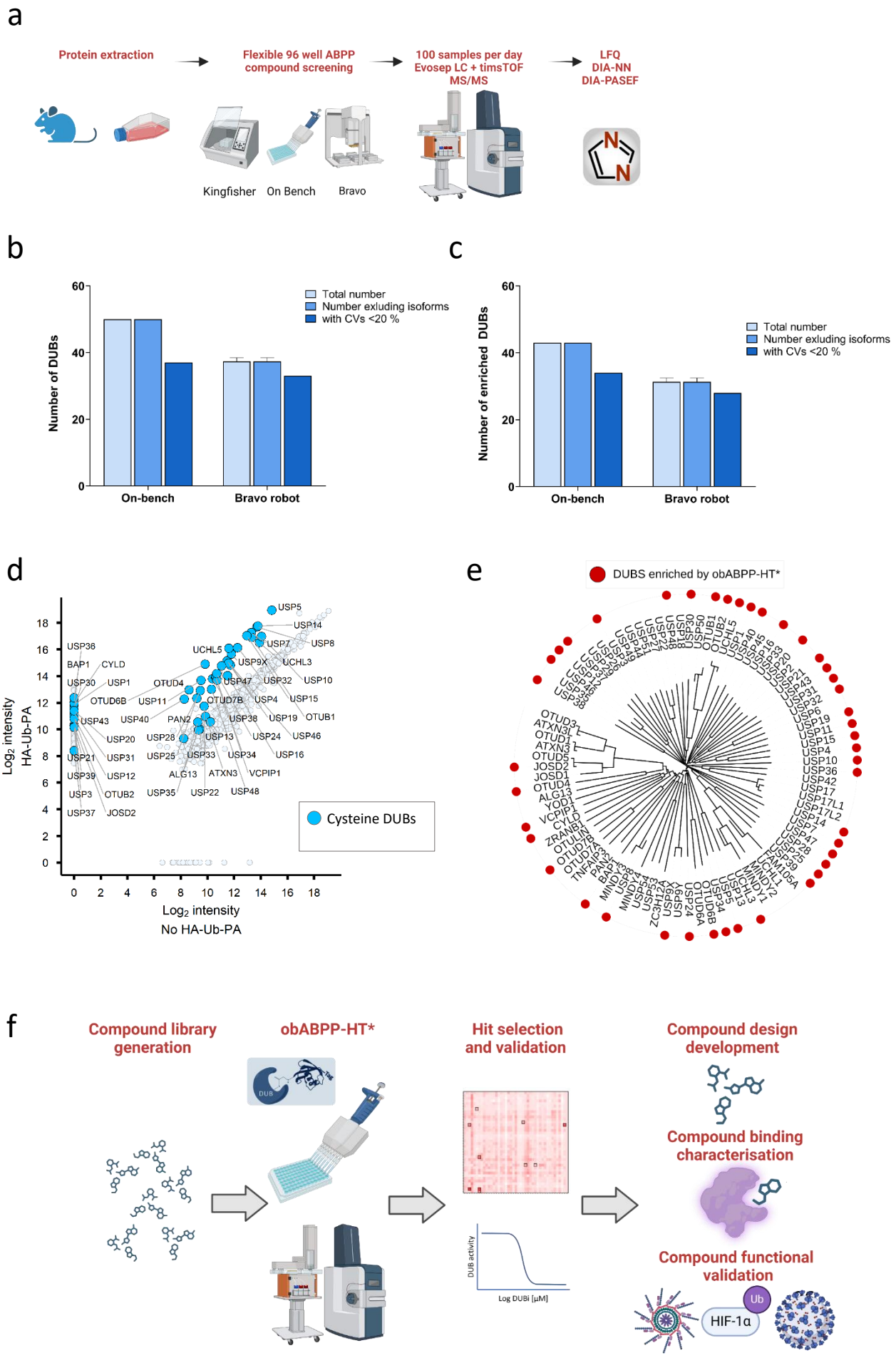

a, HA-Ub-PA high-throughput workflows. Created in BioRender. Jones, H. (2025) https://BioRender.com/yl1zds3. **b-c**, The number of cysteine-active DUBs identified from MCF-7 cell lysates by ABPP in total (**b**), or enriched > 5-fold compared to a negative control (**c**) using the high-throughput workflows outlined in **a**, with on-bench or Bravo robot 96-well immunoprecipitation (error bars = standard deviation (SD)). **d**, Enrichment of cysteine-active DUBs with the obABPP-HT* methodology. **e**, Phylogenetic tree of cysteine-active DUBs, with those enriched by the obABPP-HT* methodology denoted with red circles. The phylogenetic tree was generated with clustal omega multiple sequence alignment[84], and visualised using iTOL[85]. **f**, obABPP-HT* DUB inhibitor screen workflow. Created in BioRender. Jones, H. (2025) https://BioRender.com/gkv1hyo. LFQ = Label-free quantitation, DIA-PASEF = data-independent acquisition-Parallel Accumulation–Serial Fragmentation.

Fig. 2 DUB inhibitor screen using *ob*ABPP-HT*.

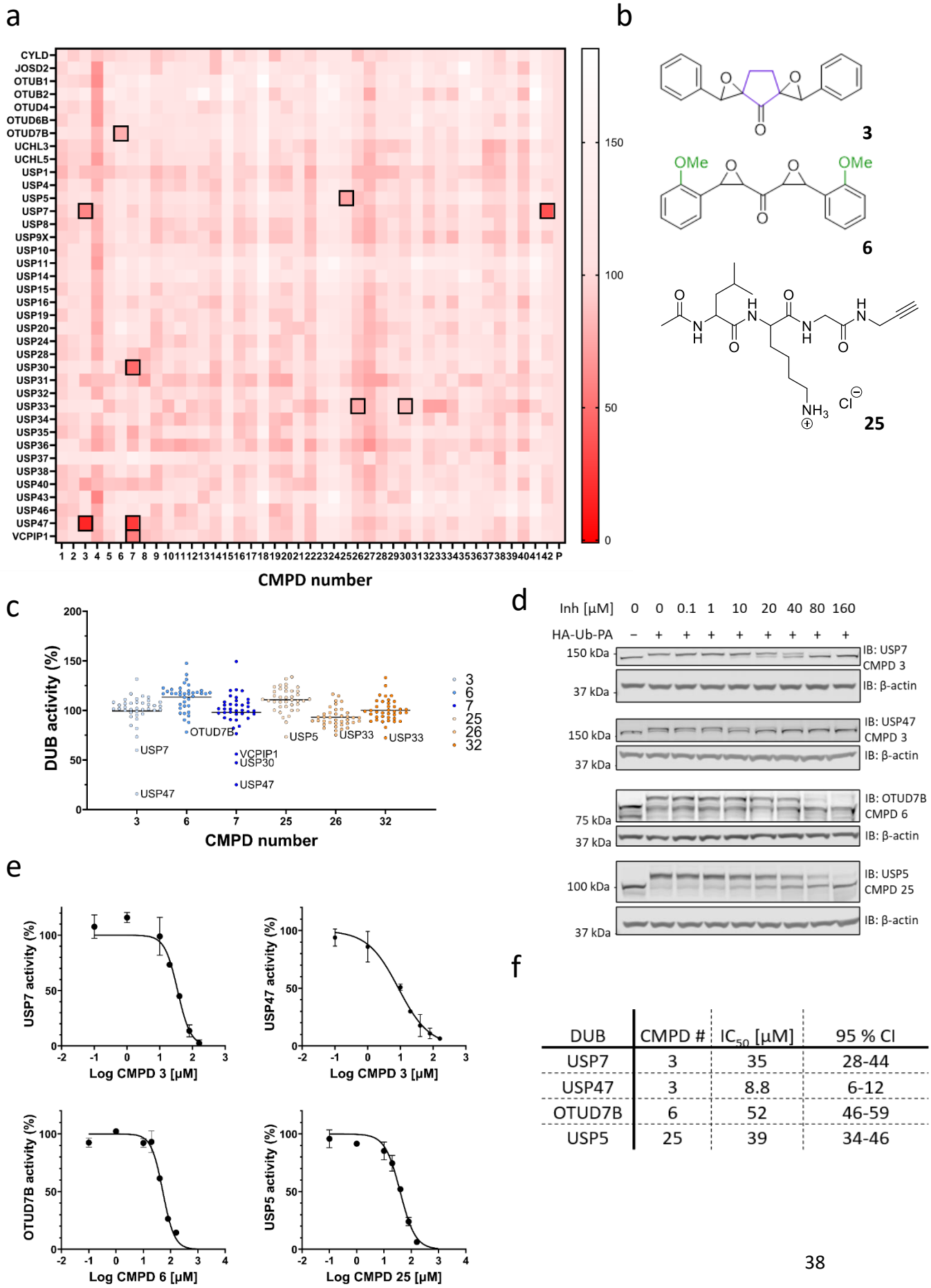

f

DUB	CMPD #	IC_{50} [μM]	95 % CI
USP7	3	35	28-44
USP47	3	8.8	6-12
OTUD7B	6	52	46-59
USP5	25	39	34-46

a, Heatmap of DUBs identified from *ob*ABPP-HT* screen, performed using MCF-7 lysates. DUB activity in the presence of 25 µM of **Compounds 1-41** (**Compound 42** = established USP7 inhibitor FT827) as a % of positive control activity (n = 2, controls n = 4). Cells outlined with black squares indicate > 20 % inhibition ($p < 0.05$ - two tailed unpaired t-test, (**Compound 6** OTUD7B p= 0.066)), with significant inhibition from **Compounds 4** and **27** not highlighted due to lack of selectivity. **b**, Compound structures of positive hits. **c,** Significant hits from **a** taken forward for validations, showing reduction in activity relative to other DUBs. **d**, HA-Ub-PA ABP validations in MCF-7 cell lysates showing concentration-dependent inhibition of DUBs by positive hits identified from *ob*ABPP-HT* screen. **e**, Densitometric quantitation from western blots of positive hits (n = 2) showing log inhibitor concentration *vs* normalised DUB activity, fit to Y=100/(1+10^((LogIC_{50}-X)*HillSlope)) (error bars = SD). **f**, IC_{50} values extracted from fits in e, (CI= Confidence interval).

Fig. 3 Hit profiling using *ob*ABPP-HT* and cellular permeability.

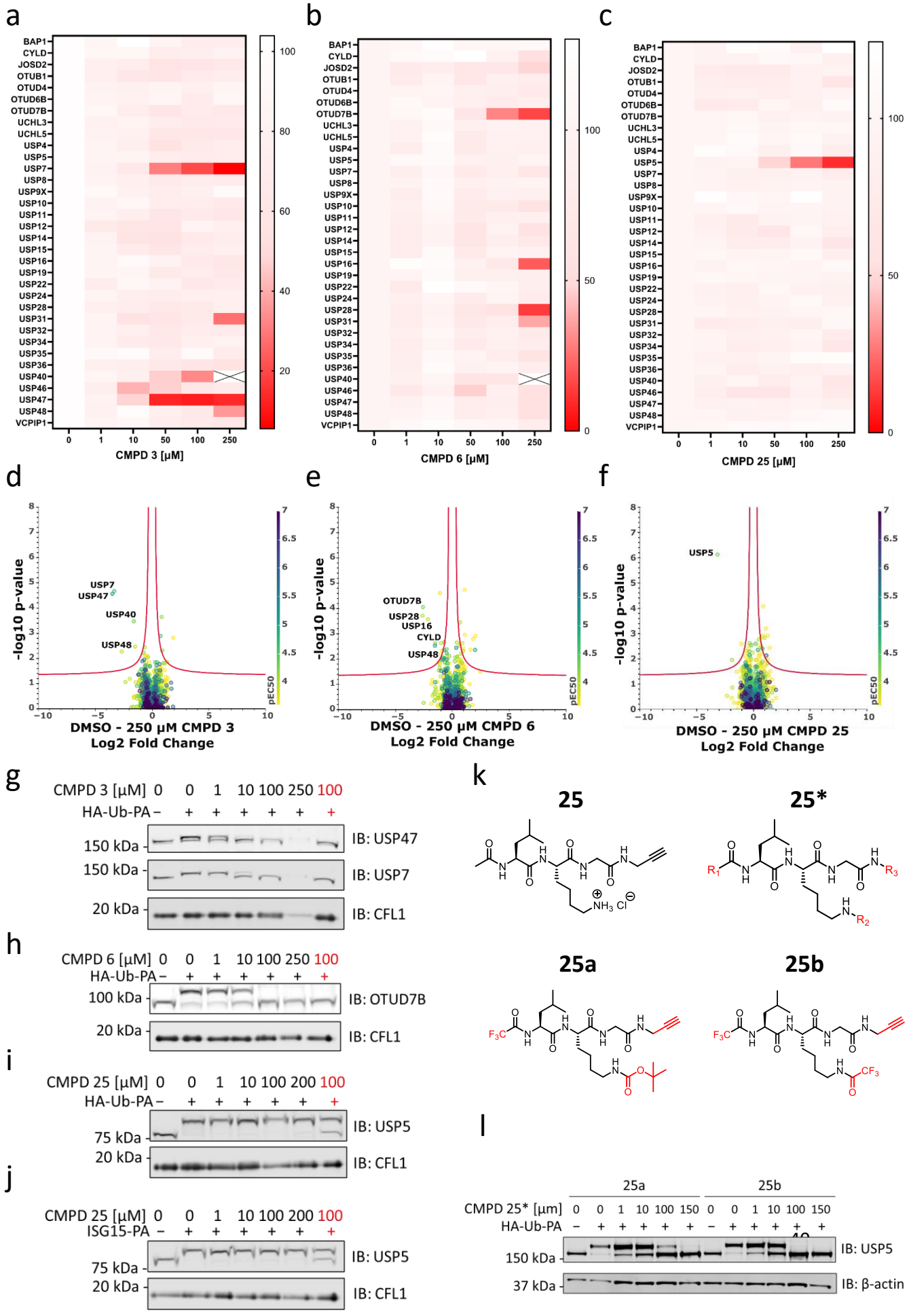

1169 **a-c**, *ob*ABPP-HT* DUB activity with concentration-dependence of **Compounds 3** (**a**), **6** (**b**) and
1170 **25** (**c**) (n = 2, controls n = 3). **d-f**, Curve curator volcano plots[75], showing Log2 Fold change
1171 decrease in DUB intensity with 250 µM of **Compound 3** (**d**), **6** (**e**), and **25** (**f**). Colour is reflective
1172 of pEC_{50} values across concentration-dependence shown in in a-c. **g-j**, Cell permeability
1173 concentration-dependence of **Compounds 3**, **6** and **25** after incubation with MCF-7 cells for 4
1174 h, lysis and subsequent labelling with HA-Ub-PA or ISG15-PA. **k**, Varying the R1 and R2 groups
1175 of **Compound 25** enhances cellular permeability. **l**, Cellular permeability concentration-
1176 dependence of USP5 inhibition with **Compounds 25a** and **25b** after incubation with MCF-7
1177 cells for 4 h, lysis and subsequence labelling with HA-Ub-PA.

1178

1179

1180

1181

1182

1183

1184

1185

1186

1187

1188

1189

1190

1191

1192

1193

1194

1195

1196

1197

1198

1199

1200

Fig. 4 Molecular Basis for Selective Inhibition of USP47 by Compound 3.

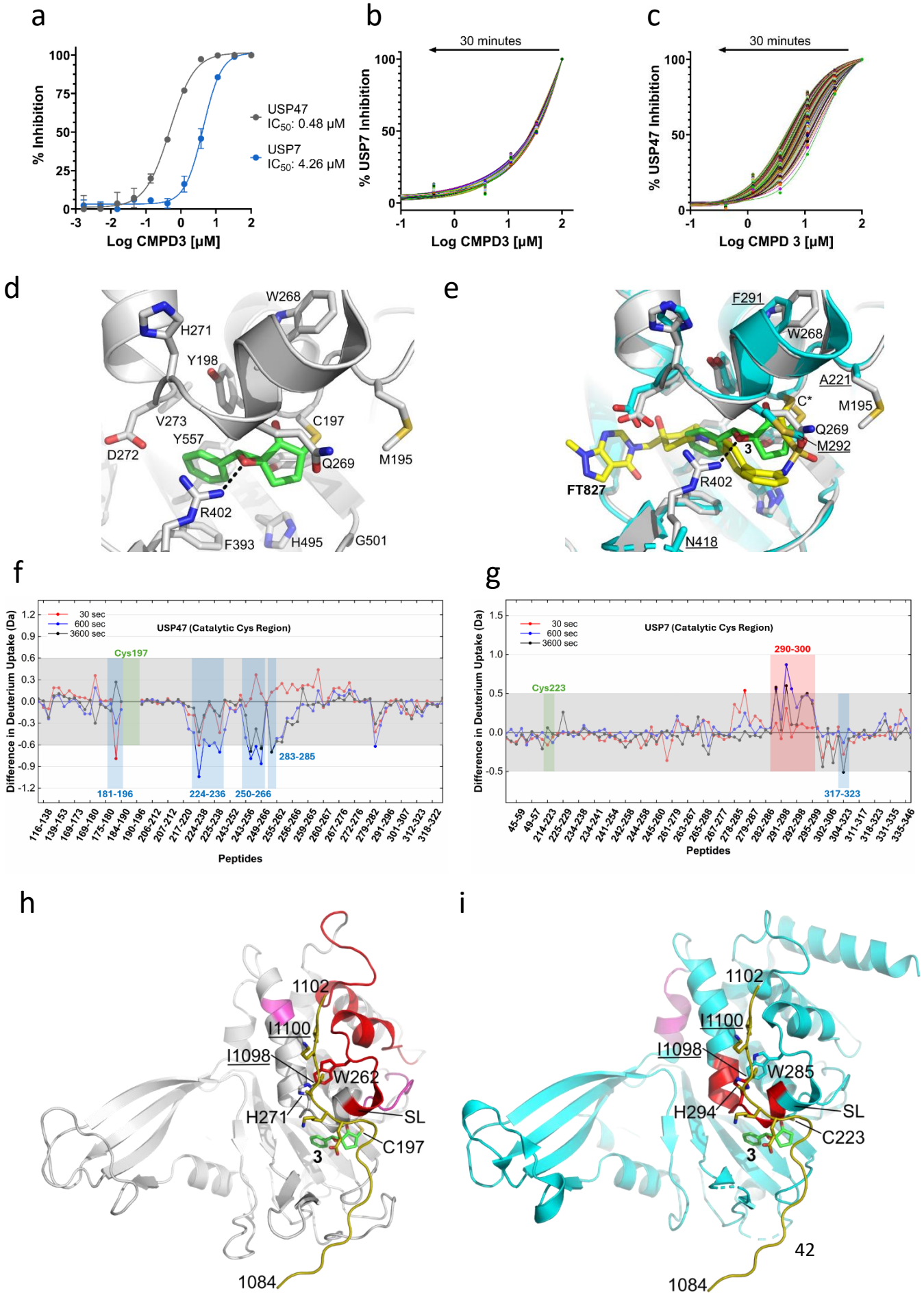

a, Inhibition of purified USP47 and USP7 determined from Ub-Rho cleavage after a 30 min pre-incubation with varying concentrations of **Compound 3**. IC_{50} curves fit to: Y=Bottom + (Top-Bottom)/(1+10^((LogIC_{50}-X)*HillSlope)) (Error bars = SD). **b**, Inhibition of USP47 with **Compound 3** without preincubation, determined from Ub-Rho cleavage. Each curve represents inhibition data at an individual incubation time from 18 to 1782 s. **c**, Inhibition of USP7 with **Compound 3** without pre-incubation, determined from Ub-Rho cleavage. Each curve represents inhibition data at an individual incubation time from 18 to 1782 s. **d**, Modelled structure of human USP47 in complex with **Compound 3**, shown as a stick representation with carbon atoms coloured green. Residues within 5 Å of the **Compound 3**-C197 adduct are highlighted, and the key hydrogen-bonding interaction between the epoxide moiety of **Compound 3** and the side chain of R402 is represented as a dotted line. Figure prepared using PyMOL (The PyMOL Molecular Graphics System, version 2.5.8; Schrödinger, LLC). **e**, Superposition of the modelled structure of human USP47 (grey) in complex with **Compound 3** (green carbon atoms) on the X-ray structure of human USP7 (cyan) in complex with the covalent inhibitor, FT827 (yellow carbon atoms; PDB: 5NGF). C* denotes the catalytic cysteine (corresponding to C197 in human USP47 and C223 in human USP7). **Compound 3** is predicted to bind within the thumb-palm cleft in a similar fashion to FT827, with FT827 extending out further towards the fingers subdomain. Sequence differences are labelled for human USP47 and the corresponding residues are labelled and underlined for human USP7. R402 in USP47 is predicted to hydrogen bond directly to **Compound 3** (represented as a dotted line). R402 in USP47 corresponds to N418 (disordered side chain in PDB: 5NGF) in USP7 with a shorter side chain that cannot interact with the compound, which may explain the higher potency of **Compound 3** for USP47. Residual ΔHDX plots showing differences in deuterium uptake between holo- and apo- states for USP47 (**f**) and USP7 (**g**), across all indicated peptide fragments and time points (30 sec to 1 h). These zoomed-in views highlight the peptides surrounding only those regions of the full-length protein (residues 116-323 of USP47 (**f**) and 45-347 of USP7 (**g**)). These regions also encompass the catalytic cysteine residue of each DUB. Positive ΔHDX values indicate increased solvent exposure or flexibility in the presence of **Compound 3**, whilst negative values suggest protection or structural stabilisation. A grey shaded area marks the significance threshold for ΔHDX applied in each study. The green boxes indicate those peptides which encompass the catalytic cysteine. Due to the disappearance of these peptides in the holo-state of USP47, these peptides could not be visualised on the plot. This is further evidence of the covalent attachment of **Compound 3** to the catalytic cysteine in USP47. **h**, Modelled structure of human USP47 catalytic domain (grey) in complex with **Compound 3** (carbon atoms in green) highlighting regions identified in the HDX-MS analysis coloured red (mean perturbation over 60 min of 5–20%) and magenta (mean perturbation over 60 min of <60%). The 19-residue C-terminal activation peptide of human USP7 (PDB: 5JTV; corresponding to residues 1084 to 1102) is shown in gold with key residues labelled and underlined. The activation peptide of USP47 (corresponding to residues 1345 to 1362)[33] is proposed to play an important role in activation and regulation analogous to the activation peptide of USP7, which maintains the switching loop (SL; especially W285 and H294) in the active "out" conformation[34]. W285 and H294 in human USP7 correspond to W262 and H271 in human USP47. Regions identified in the USP47 HDX-MS analysis correlate with a conformational shift in the SL and potential engagement of the activation peptide upon

Compound 3 binding. **i**, Human USP7 catalytic domain (cyan; from PDB: 5NGF) with the superimposed modelled position of **Compound 3** in human USP47 (green carbon atoms) highlighting regions identified in the HDX-MS analysis coloured red (mean perturbation over 60 min of 5–20%) and magenta (mean perturbation over 60 min of <60%). The 19-residue C-terminal activation peptide of human USP7 (PDB: 5JTV; corresponding to residues 1084 to 1102) is shown in gold with key residues labelled and underlined. Analysis of human USP7 HDX-MS data reveals that the region of highest confidence directly flanks the proposed compound binding site and differences are not observed in structural elements implicated in activation peptide binding, suggesting that **Compound 3** does not trigger an equivalent shift in SL to the active "out" conformation and subsequent binding of the activation peptide as predicted for USP47.

Fig. 5 Functional validation of compounds 3, 6 and 25b.

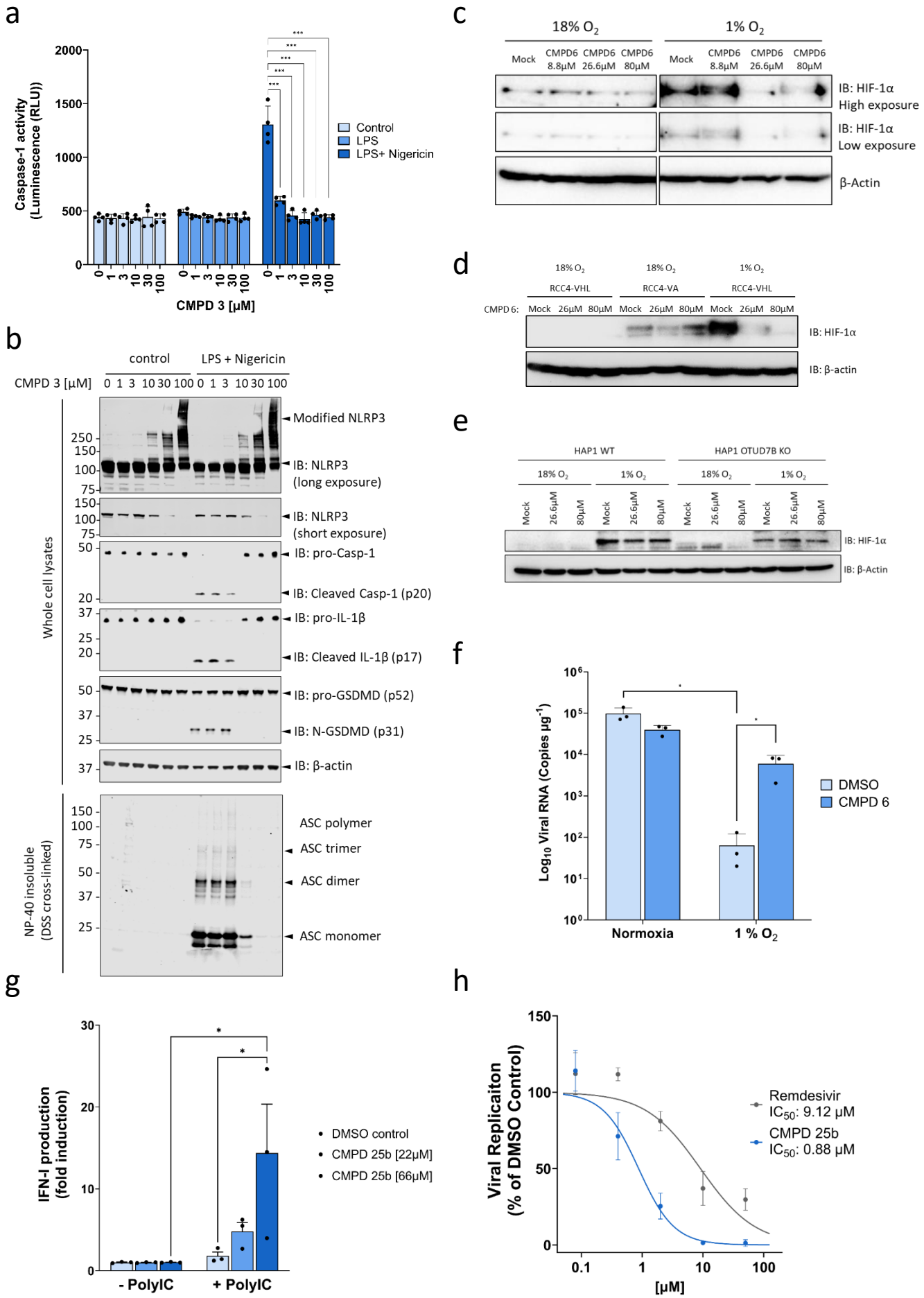

1336 **a**, Caspase-1 activity in the media (supernatant) of PMA-differentiated THP-1 cells treated
1337 with indicated concentrations of **Compound 3**, determined using Caspase-Glo 1 luminescence
1338 assay. **Compound 3** incubation for 4 h, ± 1 µg/mL LPS incubation for 4 h and 10 µM Nigericin
1339 incubation for 45 min (error bars = SD). One-way ANOVA was used. ***P < 0.001. **b**,
1340 Immunoblots of NLRP3, Caspase-1 (Casp-1), and gasdermin d (GSDMD) from whole cell
1341 lysates of PMA-differentiated THP-1 cells treated with indicated concentrations of **Compound**
1342 **3**. Immunoblot of ASC oligomerisation of the NP40-insoluble fraction of PMA-differentiated
1343 THP-1 cells after treatment with the indicated concentrations of **Compound 3** and DSS cross-
1344 linking. **Compound 3** incubation for 4 h, ± 1 µg/mL LPS incubation for 4 h and 10 µM Nigericin
1345 incubation for 45 min. **c**, Immunoblot of HIF-1a in Calu-3 cells incubated in 18% or 1% O_2 for
1346 24 h followed by treatment with increasing doses of **Compound 6** for 1h. **d**, expression of
1347 HIF-1a in RCC4-VA (Mutant VHL) or –VHL (Wt VHL) cells treated with increasing doses of
1348 **Compound 6**. Lysates from hypoxic RCC4-VHL cells treated with **Compound 6** were also
1349 performed to induce HIF-1a expression. **e**, HAP1-WT and OTUD7B KO cells were incubated in
1350 18% or 1% O_2 for 24 h followed by treatment with indicated doses of **Compound 6** for 1 h.
1351 HIF-1α expression was then determined by immunoblot in WT and KO cells. **f,** Calu-3 cells
1352 were infected with SARS-CoV-2 (VIC02/20) at a multiplicity of infection (MOI) of 0.01 for 1h.
1353 The inoculum was removed and cells incubated at 18% or 1% O_2 for 24 h treated with or
1354 without 26.6 µM of **Compound 6**. Viral replication was quantified by qPCR of intracellular viral
1355 RNA and expressed as copies µg-1 of total cellular RNA. Data is representative of three
1356 biological replicates and data presented as mean -/+ S.D. Significance from Mann-Whitney
1357 test, * = p < 0.0332. **g**, Interferon I (IFN-I) production by HAP1 cells treated with **Compound**
1358 **25b**/DMSO for 1 hour, followed by poly(I:C) (0.5 µg/mL) for 48 h. HEK293 IFN reporter cells
1359 were incubated with HAP1 media for 24 h, and luminescence determined with the One-Glo
1360 luciferase assay system. Data is representative of three replicates with data presented as
1361 mean -/+ SEM. Significance from 2-way ANOVA, with Tukey's multiple comparisons test, * =
1362 p < 0.0332 **h**, Calu-3 cells were infected with SARS-CoV-2-mNeonGreen reporter virus at a
1363 MOI of 0.1 and treated with a range of doses of the USP5 inhibitor **Compound 25b** or
1364 Remdesivir[86]. Data is representative of three biological replicates and data presented as mean
1365 -/+ SEM. Dose response curves were determined using a non-linear regression analysis to
1366 calculate IC_{50} values for each compound.

1367

1368

1369

1370

1371

1372

1373

1374

Extended Data

1394 **Extended Data Fig. 1: ABPP optimisation and flexibility.**

1395

1396

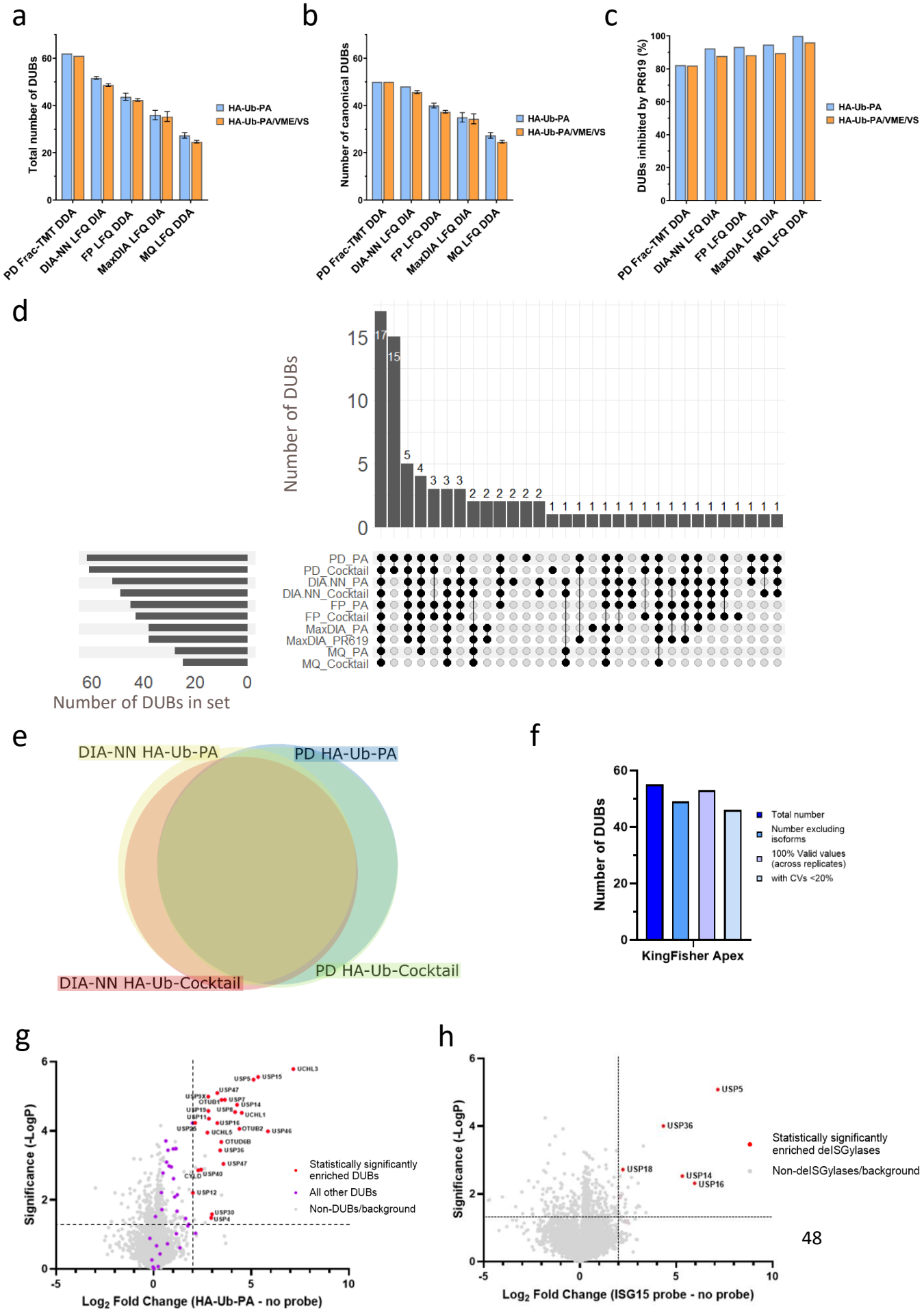

1397 **a-b**, Comparison of the total number of DUBs, including isoforms (a) and canonical DUBs (b),
1398 identified from MCF-7 lysates by ABPP using either a propargylamine warhead (HA-Ub-PA) or
1399 a mixture of propargylamine, vinyl methyl ester (VME) and vinyl sulfone (VS) warheads, using
1400 ultra-sensitive ABPP workflows (error bars = SD). **c**, Percentage of DUBs inhibited >50% by
1401 PR619 from each ABPP workflow. **d**, Upset plot showing the commonality of DUBs identified
1402 from MCF-7 cell lysates by each high DUBome depth workflow including isoforms. **e**,
1403 Comparison of the identities of canonical DUBs identified from MCF-7 lysates using proteome
1404 discoverer (PD) from data-dependent acquisition (DDA) tandem mass tagged (TMT) labelled
1405 fractionated ABPP samples, or data-independent acquisition (DIA)-NN DIA non-fractionated
1406 label-free ABPP samples, using HA-Ub-PA or HA-Ub-PA/VME/VS (cocktail). Frac: high pH
1407 fractionated; LFQ: Label-free quantitation; FP: FragPipe; MQ: Maxquant. **f-g,** The number of
1408 DUBs identified from HAP1 lysates by ABPP in total (f), and in terms of statistical significance
1409 as illustrated on a volcano plot (g) using the ABPP-HT* high-throughput workflow with
1410 KingFisher Apex 96 well automated affinity purification. **h,** Enrichment of DUBs in HAP1
1411 lysates by bio-ISG15-PA ABPP using the ABPP-HT* workflow with Kingfisher Apex 96 well
1412 automated affinity purification.

1413

Extended Data Fig. 2: Hit Validation and Dose-response Analysis.

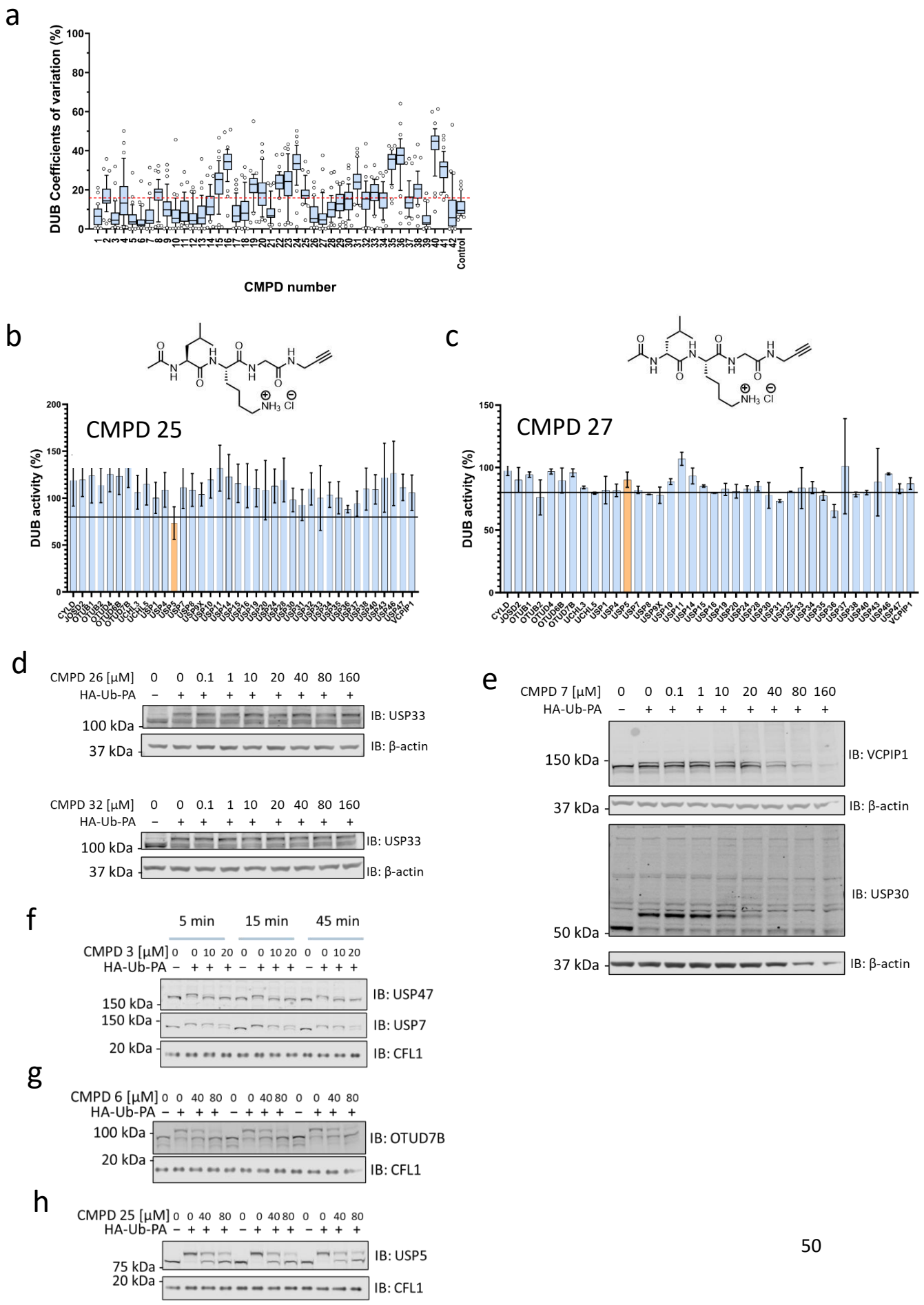

a, Coefficient of variation (CV) for DUBs identified across the *ob*ABPP-HT* screen for each of the tested compounds. Box and whiskers are at 10-90 percentile. Red dashed line: average CV for DUBs across all conditions. **b-c**, HA-Ub-PA ABPP of **Compounds 25** and **27** at 25 µM in MCF-7 cell lysates (error bars = SD). **d**, Concentration-dependent binding of **Compounds 26** and **32** to USP33 in MCF-7 cell lysates. Data was obtained using with HA-Ub-PA as ABP. **e**, Concentration-dependent for VCPIP1 in MCF-7 lysates and USP30 in SH-SY5Y lysates by **Compound 7** with HA-Ub-PA labelling. The observation of high-molecular weight smearing and reduced intensity of DUBs suggests that **Compound 7** mediated DUB cross-linking. **f-h**, Time-dependent incubation of MCF-7 lysates at the indicated compound concentrations using HA-Ub-PA labelling.

Extended Data Fig. 3: DUB Inhibitor Selectivity Assessment by *ob*ABPP-HT*.

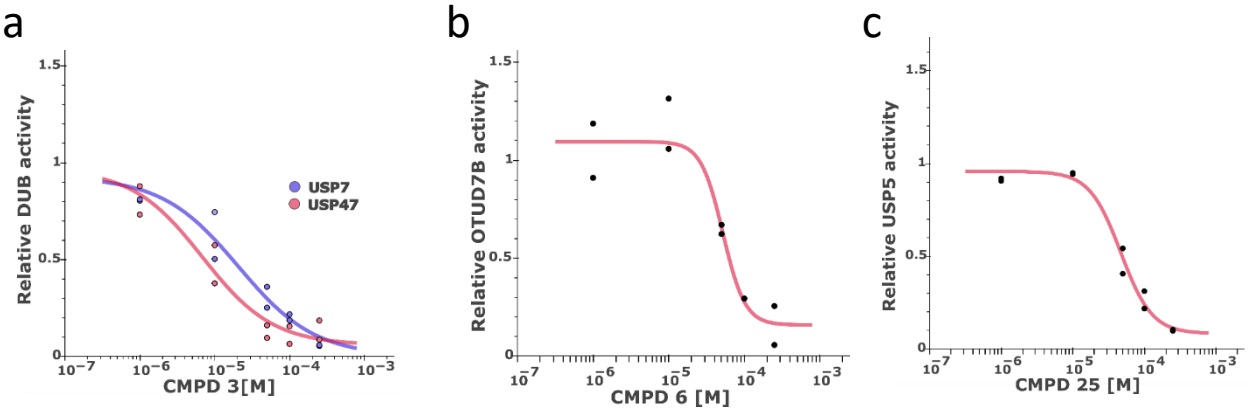

d

DUB	CMPD #	IC_{50} [µM]	R^2
USP7	3	20.70141	0.85
USP47	3	6.854882	0.85
OTUD7B	6	52.23962	0.819
USP5	25	46.88134	0.96

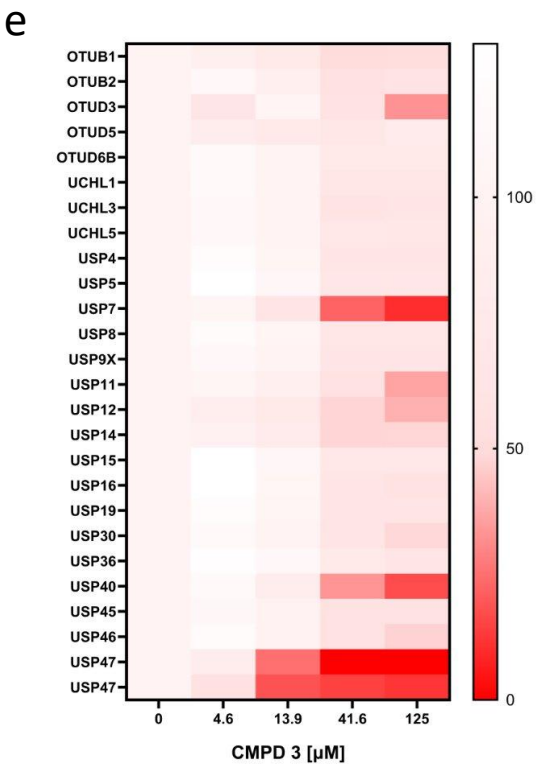

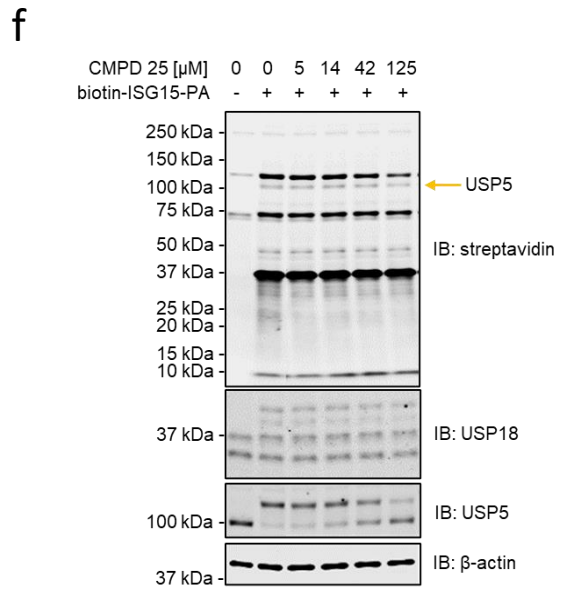

a-c, Concentration-dependent compound binding to DUBs identified using *ob*ABPP-HT*, with HA-Ub-PA. Data were analysed using curve curator[75]. **d,** IC_{50} values obtained using curve curator from the curves shown in a-c. **e,** Concentration-dependent binding of **Compound 3** to DUBs in HAP-1 lysates determined using high-throughput KingFisher Apex ABPP with HA-Ub-

1482 PA. **f, Compound 25** concentration dependence bio-ISG15-PA ABP with USP5 and USP18 in
1483 lysates from HAP1 cells treated with 1000 U/mL of human interferon α 2 (α2b) for 24 h.

1484

1485

1486

1487

1488

1489

1490

1491

1492

1493

1494

1495

1496

1497

1498

1499

1500

1501

1502

1503

1504

1505

1506

1507

1508

1509

1510

1511

Extended Data Table 1: Structure-activity relationship (SAR) of Compound 25 to increase cellular permeability.

	R_1	R_2	R_3	Cell permeable	USP5 inhibition in lysates
25c	Me	NHBoc	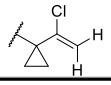	N	N
25d	Me	NHBoc		N	Y
25e	Me	NHBoc		N	N
25f	Me	NHBoc		N	N
25g	Me	NHBoc	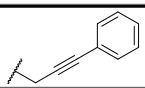	N	N
25h	Me	NH_3Cl		N	N
25i	Me	NH_3Cl	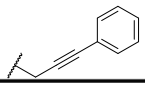	N	N
25j	Me	NH_3Cl		N	N
25a	CF_3	NHBoc		Y	Y
25k	CF_3	NH_3Cl		N	Y
25b	CF_3	NHTrifluoro acetyl		Y	Y

Effects on alterations of the R1, R2 and R3 groups of **Compound 25** on cell permeability and USP5 binding using HA-Ub-PA assays.

Extended Data Fig. 4: Selective inhibition of USP5 by compounds 25, 25a and 25b

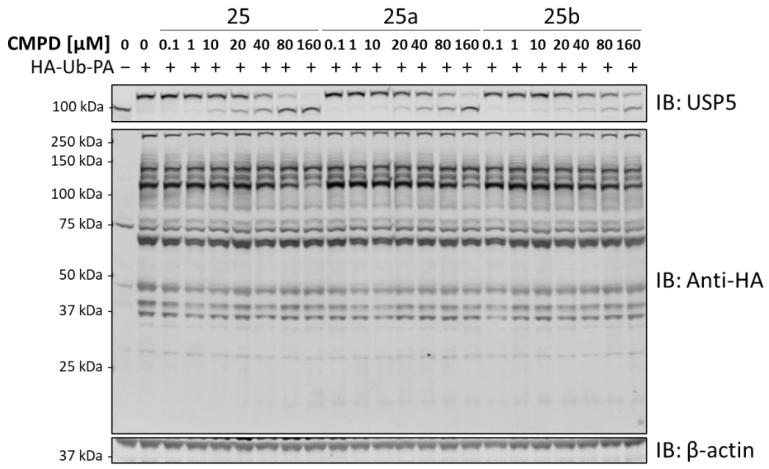

1544 HA immunoblot showing concentration-dependent selective binding of **Compounds 25**, **25a**
1545 and **25b** to USP5 in MCF-7 cell lysates using HA-Ub-PA ABP.

1546

1547

1548

1549

1550

1551

1552

1553

1554

1555

1556

1557

1558

1559

1560

1561

1562

1563

1564

1565

1566

1567

1568

1569

1570

1571

1572

1573

1574

1575 **Extended Data Fig. 5. Molecular Basis for Selective Inhibition of USP47 by Compound 3.**

1576

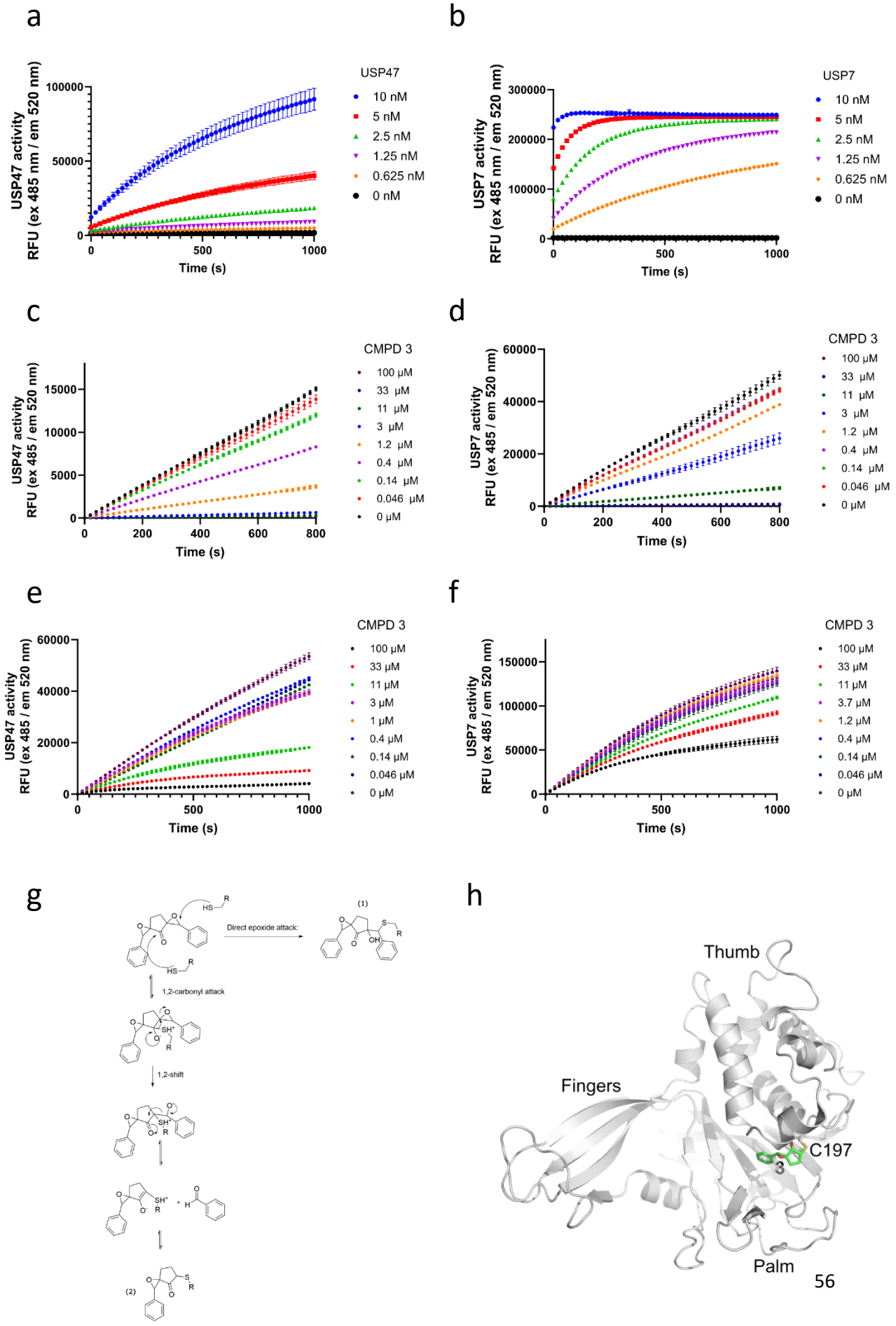

1577

i

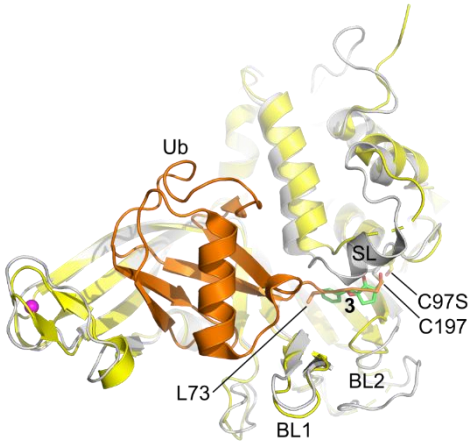
Ub
SL
3
C97S
C197
L73
BL2
BL1

j

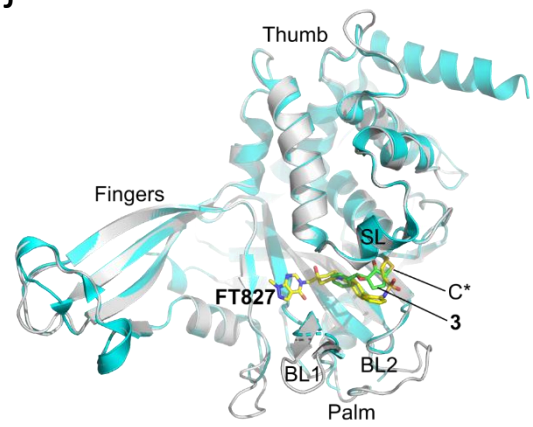
Thumb
Fingers
SL
FT827
C*
3
BL1
BL2
Palm

k

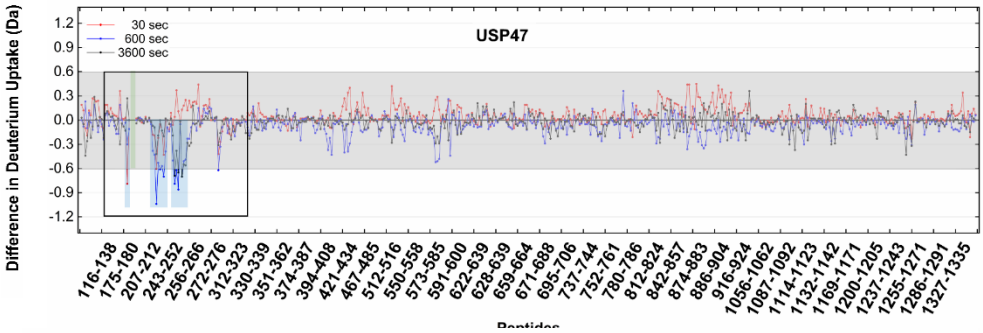
USP47
30 sec
600 sec
3600 sec
Difference in Deuterium Uptake (Da)
1.2
0.9
0.6
0.3
0.0
-0.3
-0.6
-0.9
-1.2
116-138
175-180
207-212
243-252
256-266
272-276
312-323
330-339
351-362
374-387
394-408
421-434
467-485
512-516
550-558
573-585
591-600
622-639
628-639
659-664
671-688
695-706
737-744
752-761
780-786
812-824
842-857
874-883
886-904
916-924
1056-1062
1087-1092
1114-1123
1132-1142
1169-1171
1200-1205
1237-1243
1255-1271
1286-1291
1327-1335

l

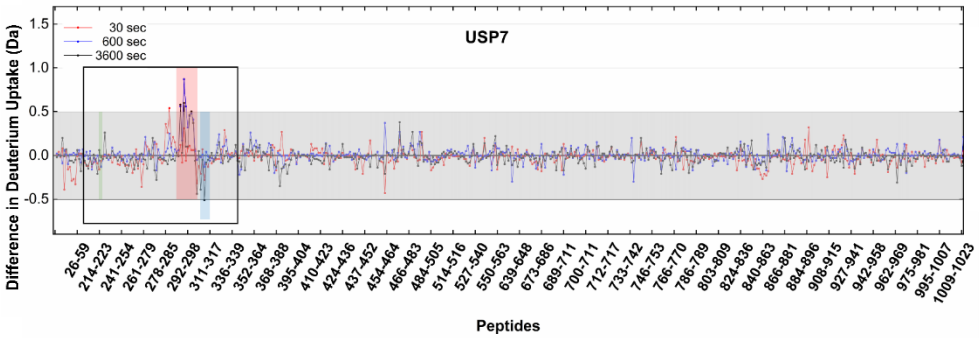
USP7
30 sec
600 sec
3600 sec
Difference in Deuterium Uptake (Da)
1.5
1.0
0.5
0.0
-0.5
26-59
214-223
241-254
261-279
278-285
292-298
311-317
336-339
352-364
368-388
395-404
410-423
424-436
437-452
454-464
466-483
484-505
514-516
527-540
550-563
639-648
673-686
689-711
700-711
712-717
733-742
746-753
766-770
786-789
803-809
824-836
840-863
865-881
884-896
908-915
927-941
942-958
962-969
975-981
995-1007
1009-1023
Peptides

m

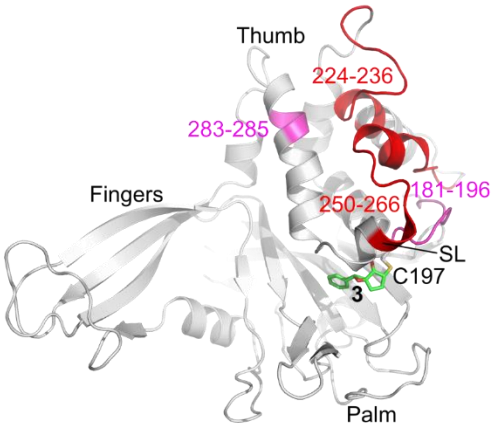
Thumb
224-236
283-285
Fingers
181-196
250-266
SL
C197
3
Palm

n

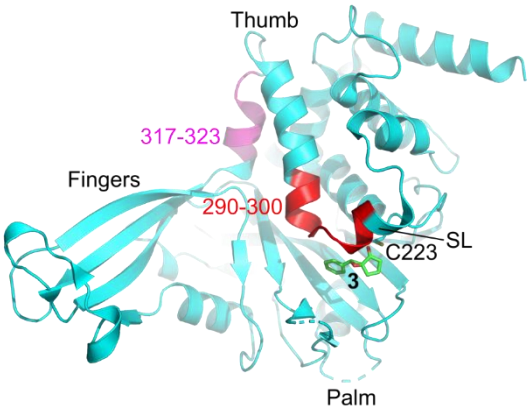
Thumb
317-323
Fingers
290-300
SL
C223
3
Palm

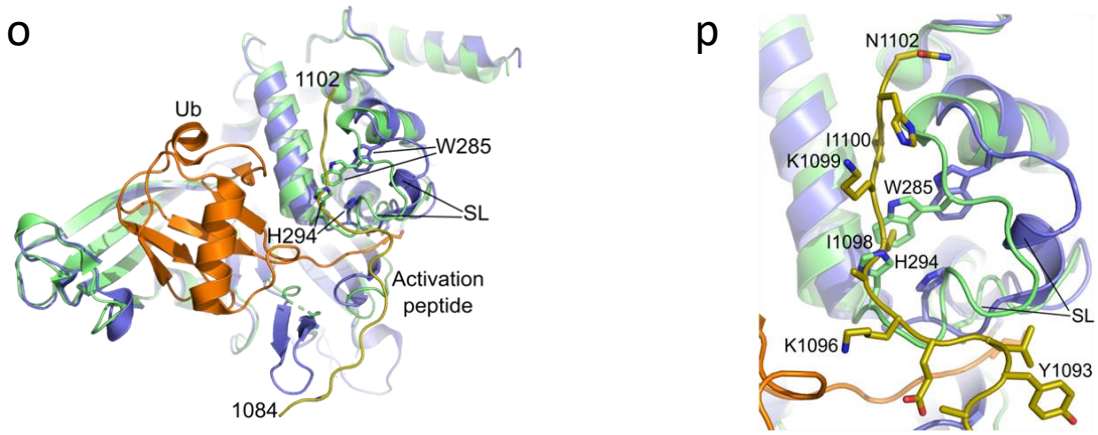

a-b, Progress curves showing (a) USP47- and (b) USP7-catalysed hydrolysis of Ub-Rho over time (error bars represent SD). **c-d**, Progress curves showing (c) USP47- and (d) USP7-catalysed hydrolysis of Ub-Rho in the presence of varying concentrations of **Compound 3**, following preincubation of USP47 or USP7 with **Compound 3** for 30 min (error bars: standard error of the mean (SEM)). **e-f**, Progress curves showing (e) USP47- and (f) USP7-catalysed hydrolysis of Ub-Rho in the presence of varying concentrations of **Compound 3**, without preincubation (error bars: SEM). **g,** Proposed mechanism of the covalent reaction of **Compound 3** with the catalytic cysteine C197 of human USP47. At least two alternative mechanisms for the reaction of **Compound 3** with the catalytic cysteine are plausible, with the reaction proceeding via 1,2-carbonyl attack and retro-aldol fragmentation to form (2) being the most probable based on previous observations using a related diepoxide[26]. **h,** Modelled structure of human USP47 in complex with **Compound 3** shown as a stick representation with carbon atoms colored green. The thumb, palm and fingers subdomains of the catalytic domain and the catalytic cysteine, Cys197, are highlighted. Figure prepared using PyMOL (The PyMOL Molecular Graphics System, version 2.5.8; Schrödinger, LLC). **i,** Superposition of the modelled structure of human USP47 in complex with **Compound 3** on the X-ray structure of *C.elegans* USP47 in complex with ubiquitin (PDB code: 8ITP[33]). The thumb, palm and fingers subdomains, the *C.elegans* USP47 catalytic cysteine point mutation (C97S), and the catalytic cysteine in the human USP47 model (Cys197) are highlighted. The catalytic domain of the modelled structure of human USP47 in complex with **Compound 3** is colored grey, and **Compound 3** is shown with carbon atoms colored green. The catalytic domain of *C.elegans* USP47 in complex with Ub is colored yellow with Ub shown in orange. **Compound 3** is predicted to bind in the thumb-palm cleft that is reported to guide the ubiquitin C-terminus into the active site. The positions of BL1, (BL2), and SL are highlighted. **j,** Superposition of the modelled structure of human USP47 (grey) in complex with **Compound 3** (green carbon atoms) on the X-ray structure of human USP7 (cyan) in complex with the covalent inhibitor **FT827** (yellow carbon atoms; PDB code: 5NGF[28]). The thumb, palm and fingers subdomains, and positions of blocking loops 1 and 2 (BL1, BL2) and switching loop (SL) are highlighted. C* denotes the catalytic cysteine (corresponding to C197 in human USP47 and C223 in human USP7). **Compound 3** is predicted to bind within the thumb-palm cleft in a

similar manner as **FT827** with **FT827** extending out further towards the fingers subdomain. **k-l,** Differential HDX-MS analysis of USP47 and USP7 in apo- and holo-states. A total of 491 peptides covering 88.2% of the full-length USP47 protein sequence were identified, with an average residue redundancy of 4.2. Similarly, a total of 536 peptides covering 84.2% of the full-length USP7 sequence were identified, with an average residue redundancy of 5.9. Residual ΔHDX plots showing differences in deuterium uptake between holo- and apo- states for USP47 (k) and USP7 (l), across all mapped peptide fragments and time points (30 s to 1 h). Positive ΔHDX values indicate increased solvent exposure or flexibility in the presence of **Compound 3**, whilst negative values suggest protection or structural stabilisation. A grey shaded area marks the significance threshold for ΔHDX applied in each study. **m,** Modelled structure of human USP47 in complex with **Compound 3** (carbon atoms in green) highlighting regions identified in the HDX-MS analysis colored red (mean perturbation over 60 min of 5–20%) and magenta (mean perturbation over 60 min of <60%). The thumb, palm and fingers subdomains, catalytic cysteine (C197), and SL are labelled **n,** Human USP7 catalytic domain (from PDB code: 5NGF[28]) colored cyan with the superimposed modelled position of **Compound 3** in human USP47 (green carbon atoms) highlighting regions identified in the HDX-MS analysis colored red (mean perturbation over 60 min of 5–20%) and magenta (mean perturbation over 60 min of <60%). The thumb, palm and fingers subdomains, catalytic cysteine (C223), and SL are labelled. **o,** Structure of apoform human USP7 catalytic domain (PDB code: 1NB8[87]; lime) superimposed on the structure of the human USP7 catalytic domain from the USP7-catalytic domain-UBL45-ubiquitin complex (PDB code: 5JTV[34]; catalytic domain in violet, the C-terminal activation peptide in gold and ubiquitin in orange). The 19-amino acid activation peptide at the C-terminus of full length human USP7 stabilizes the SL (especially H294 and W285) in an active “out” conformation. **p,** Close-up view of (o) highlighting the conformational shift in SL between the inactive “in” conformation in apoform USP7 and active “out” conformation in its complex with ubiquitin.

Extended Data Fig. 6: Compound 3 inflammasome activation and toxicity.

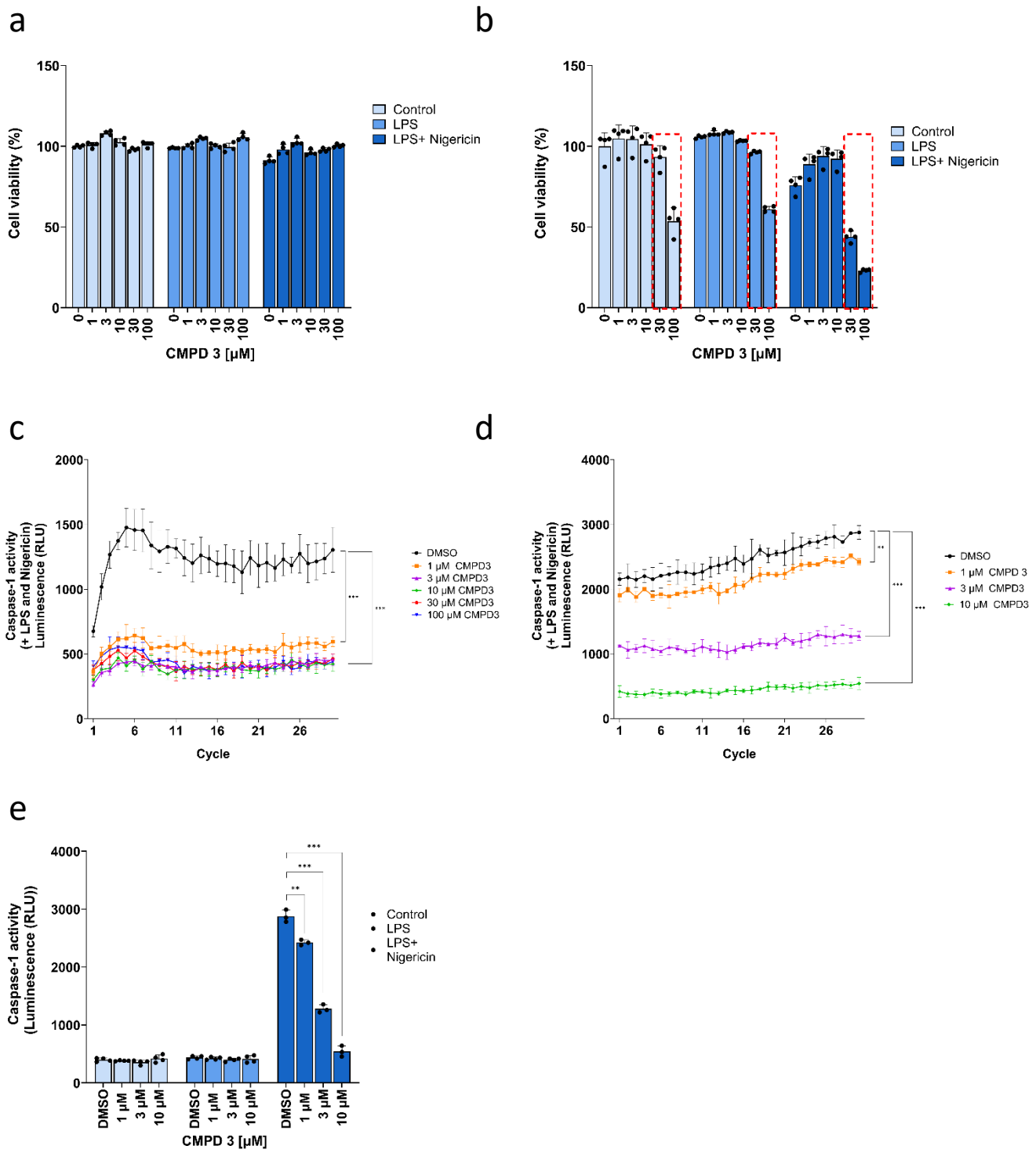

a-b, MTS cell viability of THP-1 cells treated with indicated concentrations of **Compound 3** ± LPS or LPS/Nigericin. Compound treatment for 4 h, 1 µg/mL LPS treatment for 4 h, 10 µM Nigericin treatment for 45 min (a) and 2 h (b) (error bars = SD). **c-d**, Caspase-1 activity over time in the media (supernatant) of PMA-differentiated THP-1 cells treated with indicated concentrations of **Compound 3**, determined using Caspase-Glo 1 luminescence assay.

1677 **Compound 3** incubation for 4 h, 1 µg/mL LPS incubation for 4 h and 10 µM Nigericin
1678 incubation for 45 min (c) and 2 h (d) (error bars = SD). Two-way ANOVA with Dunn's multiple
1679 comparison test was used. ***P < 0.001 **e**, Caspase-1 activity in the media (supernatant) of
1680 PMA-differentiated THP-1 cells treated with indicated concentrations of **Compound 3**,
1681 determined using Caspase-Glo 1 luminescence assay. **Compound 3** incubation for 4 h, ± 1
1682 µg/mL LPS incubation for 4 h and 10 µM Nigericin incubation for 2 h (error bars = SD).

1683

1684

1685

1686

1687

1688

1689

1690

1691

1692

1693

1694

1695

1696

1697

1698

1699

1700

1701

1702

1703

1704

1705

1706

1707

1708

Extended Data Fig. 7: Studies on cellular toxicity and molecular basis for selectivity of Compound 25b a, Compound 25b cellular toxicity.

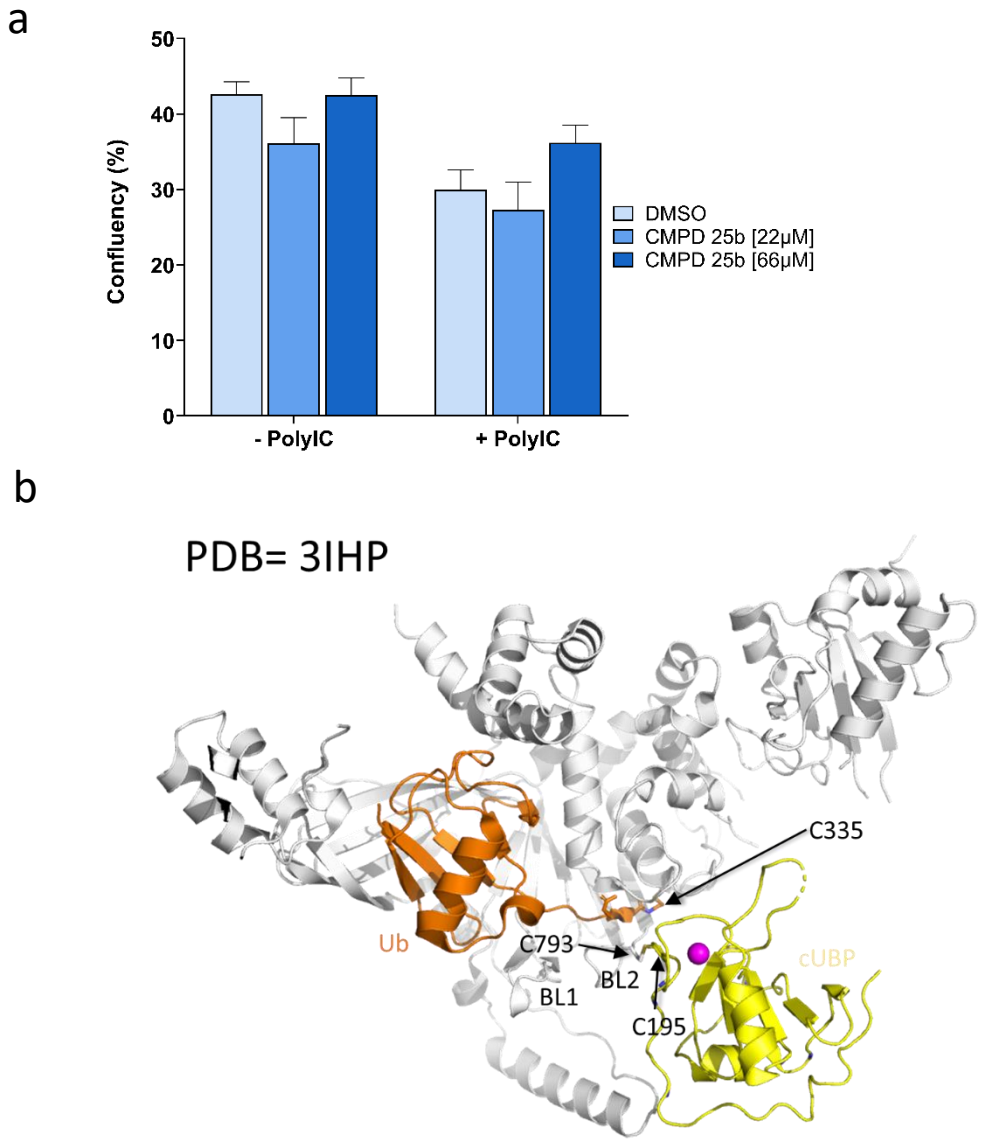

a, HAP1 cells were seeded in triplicate at 5,000 cells per well in a 96-well plate, and treated with **Compound 25b** ± Poly(I:C) 0.5 µg/mL for 48 h. Confluence at 48 h was determined by live-cell imaging using an IncuCyte SX5 machine (Sartorius) (error bars = SEM). **b**, Structure of the reported covalent USP5–Ub complex (PDB ID: 3IHP[63]) highlighting a disulphide bridge between C793 of the BL2 loop and C195 of the cUBP domain, observed in chains A and B. This tethering may restrict BL2 flexibility and position cUBP near the putative **Compound 25** binding site, potentially enabling additional interactions. As C195 is also implicated in USP5 dimerisation, the functional relevance of this disulphide bond warrants further investigation.

Extended Data Fig. 8: USP47 protein *Pan troglodytes* isoform 2 vs *Homo sapiens* isoform 1.

a

Recombinant USP47 *vs.* Canonical Human USP47
His-Tagged
14-24del
G163V
D808E
V834G
H1049Y

b

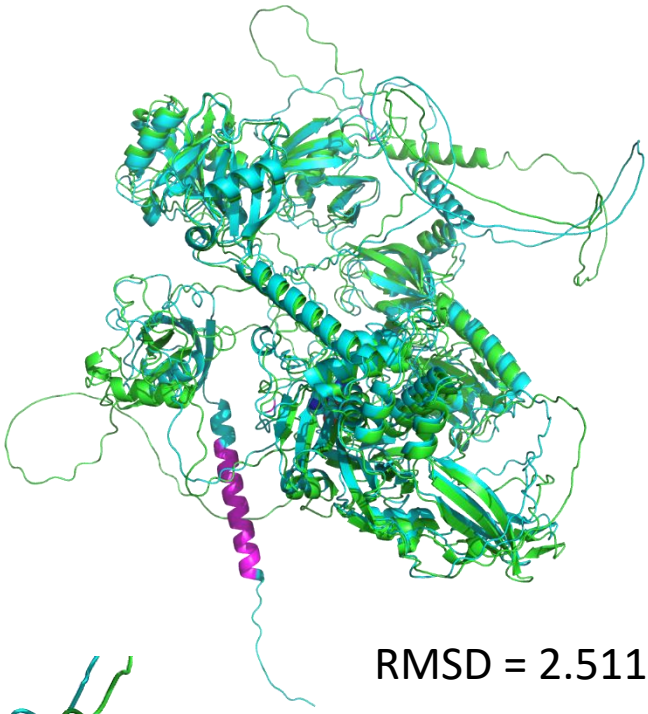

c

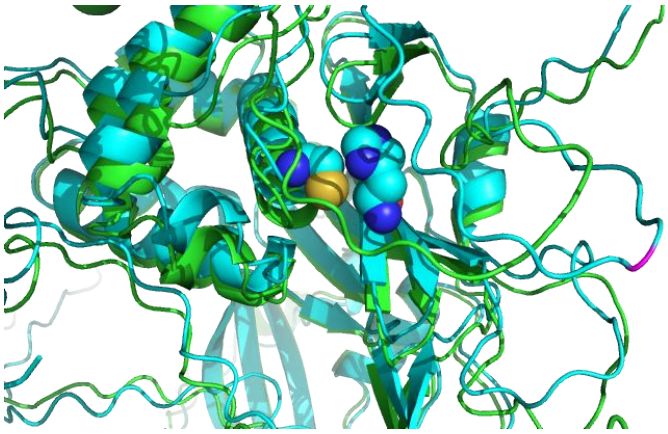

a, Sequence differences between USP47 of *Pan troglodytes* isoform 2 and canonical human USP47. **b**, Alignment of AlphaFold structures of USP47 based on *Pan troglodytes* isoform 2 used in kinetic and HDX-MS studies and canonical human USP47. Sequence differences are in pink, the catalytic cysteine 197 and histidine 503 residues are as spheres. **c**, Zoom in of alignment showing the catalytic cysteine 197 and histidine 503 residues as spheres and the nearest sequence difference in pink.